

Applications of Wavelet Methods to the Analysis of Meteorological Radar Data – An Overview

Stephan Dahlke*
Philipps–Universität Marburg
FB Mathematik und Informatik
Hans Meerwein Str., Lahnberge
35032 Marburg
Germany

Gerd Teschke†
Universität Bremen
Fachbereich 3
Postfach 33 04 40
28334 Bremen
Germany

Volker Lehmann
Deutscher Wetterdienst
Met. Observatorium Lindenberg
15864 Lindenberg
Germany

September 25, 2002

Abstract

The aim of this paper is to give an overview on the current applications of wavelet methods to the analysis of radar data. There are two major topics where wavelet algorithms have already been successfully applied, namely the reconstruction of continuous reflectivity densities and the analysis of discrete radar wind profiler data. The first problem can be treated by using the specific reconstruction and approximation properties of wavelet frames whereas the second one is treated by a suitable variant of the classical wavelet thresholding method. Both topics are discussed in detail and several numerical results are presented.

Key Words: Radar, reflectivity density, wideband regime, narrowband regime, meteorological signal processing, radar wind profiler, frames, wavelets, continuous wavelet transforms, uncertainty principles.

AMS(MOS) Subject classification: 42C15, 42C40, 65J22

*The work of this author has been supported by Deutsche Forschungsgemeinschaft (DA 360/4–1)

†The work of this author has been supported by Deutsche Forschungsgemeinschaft (MA 1657/6–1)

Contents

1	Introduction	3
2	Wavelet Analysis	4
2.1	The Discrete Wavelet Transform	5
2.2	Biorthogonal Bases	8
2.3	Continuous Wavelet Transform	9
2.4	Frames	12
3	Statistical Curve Estimation Using Wavelets	13
3.1	Threshold Wavelet Estimator	13
3.2	Error Bounds	15
4	Basic Radar Setting	15
4.1	Wideband Model	16
4.2	Narrowband Model	19
4.3	Localization and Radar Uncertainty Principles	20
4.4	Discrete Narrowband Model	21
5	Analysis of Continuous Reflectivity Densities	23
5.1	Basic Reconstruction Formulas in the Wideband Regime	24
5.2	Error Bounds in the Wideband Regime	26
5.3	Numerical Experiments in the Wideband Regime	28
5.4	Basic Reconstruction Formulas in the Narrowband Regime	31
6	Analysis of Discrete Radar Wind Profiler Data	33
6.1	Radar Wind Profilers	33
6.2	Problems in RWP Signal Processing	38
6.3	Improved RWP Signal Processing by Wavelet Techniques	39
6.4	Numerical Examples	42

1 Introduction

In recent years, wavelet analysis has become a very powerful tool in applied mathematics. The first applications of wavelets were concerned with problems in image/signal analysis/compression. Furthermore, quite recently, wavelet algorithms have also been applied very successfully in numerical analysis, geophysics, meteorology, astrophysics and in many other fields. Especially, it has turned out that the specific features of wavelets can also be efficiently used for certain problems in the context of radar signal analysis. The basic radar problem asks to gain information about an object by analyzing waves reflected from it. However, although this fundamental problem is always the same for every radar application, the algorithms that are used clearly depend on the concrete setting and may differ dramatically. The choice of the appropriate method obviously rests on the properties of the object under consideration (point object, dense target environment etc.) and on the parameters one wants to reconstruct (reflectivity densities, wind velocities etc.) For an overview on radar problems, we refer to one of the textbooks [9, 17, 22, 45, 55]. In recent studies, it has turned out that wavelet methods are at least helpful for the following two topics:

- the reconstruction of continuous reflectivity densities;
- the analysis of discrete radar wind profiler data (RWP).

The aim of this paper is to give an overview on both problems and to explain how they may be treated by wavelet methods.

The problem of reconstructing reflectivity densities can be described as follows. Let us first assume that the object under consideration can be modeled as a single point, moving with constant velocity towards or away from a given source. Then, the aim is to reconstruct the distance and the velocity of the object by analyzing the reflected waves. Indeed, for a simple point object, this goal can be achieved by simply computing the maxima of the continuous wavelet transform of the received echo, see, e.g., [30] and Section 4.1 for details. However, in many applications, one is faced with a reflecting continuum with varying reflectivities. Such a target environment is then modeled by a certain reflectivity density. In this case, this reflectivity density can *not* be reconstructed by simply transmitting one single signal, see again [30] and Section 4.1. Nevertheless, a complete reconstruction is possible if a *family* of signals is used. This approach was first suggested by Naparst [40, 41] who studied the case that the transmitted signals form an orthonormal wavelet basis. We refer to Section 2 for the definition and the basic properties of wavelets. However, the requirement of full orthonormality is quite restrictive. Therefore, quite recently, Rebollo–Neira, Plastino, and Fernandez–Rubio generalized Naparst’s approach to the case that the transmitted family forms a frame. We refer to Subsection 2.4 for a short introduction to frames. Moreover, some further generalizations concerning, e.g., rigorous error estimates, the multivariate case and numerical examples have also been presented in [10, 11]. It has turned out that especially wavelet frames perform quite successfully. The main results of these approaches are presented in Section 5.

The setting of wind profiler data is quite different. In this case, one wants to gain information concerning the three dimensional atmospheric wind vector. This is done by sampling the reflected radar beams at certain rates corresponding to different heights, followed by the application of wily

radar signal processing devices. The whole analysis consists of the following steps: coherent integration, Fourier analysis, spectral parameter estimation, and, finally, the wind estimation. The whole procedure is explained in Section 6.1. However, one of the basic problems in wind profiler analysis is that the data may be heavily contaminated by echoes returned from ground surroundings, from targets like airplanes or birds or from external radio-frequency transmissions. Due to the local nature of these disturbing signal components, de-noising algorithms based on Fourier transforms are not very appropriate. This is exactly the topic where wavelet analysis suggests itself since wavelets are by construction very localized functions. Indeed, the following variant of wavelet de-noising algorithms has already been successfully applied [32, 49]. The classical wavelet de-noising methods consist of three steps. First of all, the signal is decomposed into a wavelet series by means of the fast wavelet transform, then the small wavelet coefficients are neglected by applying some thresholding operator (hard/soft thresholding), and, finally, the signal is reconstructed by applying the inverse wavelet transform. We refer to the Sections 2 and 3 for details. However, in the setting of RWP, the disturbing components are usually much larger than the signal one wants to analyze. Therefore the thresholding operator is applied the opposite way: the small wavelet coefficients are kept and the large ones are neglected. The whole algorithm is explained in Section 6.3.

This paper is organized as follows. In Section 2, we briefly recall the basic facts on wavelet analysis as far as they are needed for our purposes. The discussion covers orthogonal and biorthogonal wavelets, the continuous wavelet transform including associated uncertainty relations, and the concept of frames. Section 3 is devoted to statistical estimations by means of wavelet methods. Then, in Section 4, we discuss the basic radar setting. We present the wideband as well as the narrowband approach. Moreover, we introduce a new discrete narrow band model which is designed to serve as some kind of bridge between the two basic problems introduced above. Then, in Section 5, we explain how a continuous reflectivity density can be reconstructed by means of a frame approach. We also present some error estimates in weighted L_2 -spaces and discuss several numerical examples. Section 6 is devoted to the radar wind profiler problems. After explaining the basic setting in Subsection 6.1, we discuss the problems in RWP signal processing in Subsection 6.2. In Subsection 6.3, we explain how wavelet methods can help to improve the current algorithms and, finally, in Subsection 6.4, we present some numerical examples.

2 Wavelet Analysis

In this section, we shall briefly recall the basic setting of wavelet analysis as far as it is needed for our purposes. First of all, in Subsection 2.1, we collect some facts concerning the discrete wavelet transform. Then, in Subsection 2.2, we discuss the biorthogonal wavelet approach. We shall also need some aspects of the continuous wavelet transform. Therefore we sketch this concept in Subsection 2.3. Finally, in Subsection 2.4, we discuss some frame techniques which will be one of the basic tools in radar analysis as we shall explain in Section 5.

2.1 The Discrete Wavelet Transform

In general, a function ψ is called a (mother) *wavelet* if all its scaled, dilated, and integer-translated versions

$$\psi_{j,k}(x) := 2^{j/2} \psi(2^j x - k), \quad j, k \in \mathbf{Z}, \quad (2.1)$$

form a (Riesz) basis of $L_2(\mathbf{R})$. Usually, these functions are constructed by means of a *multiresolution analysis* introduced by Mallat [35]:

Definition 2.1 A sequence $\{V_j\}_{j \in \mathbf{Z}}$ of closed subspaces of $L_2(\mathbf{R})$ is called a multiresolution analysis (M.R.A.) of $L_2(\mathbf{R})$ if

$$\dots \subset V_{j-1} \subset V_j \subset V_{j+1} \subset \dots; \quad (2.2)$$

$$\overline{\bigcup_{j=-\infty}^{\infty} V_j} = L_2(\mathbf{R}); \quad (2.3)$$

$$\bigcap_{j=-\infty}^{\infty} V_j = \{0\}; \quad (2.4)$$

$$f(\cdot) \in V_j \iff f(2\cdot) \in V_{j+1}; \quad (2.5)$$

$$f(\cdot) \in V_0 \iff f(\cdot - k) \in V_0 \quad \text{for all } k \in \mathbf{Z}. \quad (2.6)$$

Moreover, we assume that there exists a function $\varphi \in V_0$ such that

$$V_0 := \overline{\text{span}\{\varphi(\cdot - k), k \in \mathbf{Z}\}} \quad (2.7)$$

and that φ has stable integer translates, i.e.,

$$\|\lambda\|_{\ell_2} \sim \left\| \sum_{k \in \mathbf{Z}} \lambda_k \varphi(\cdot - k) \right\|_{L_2}. \quad (2.8)$$

The function φ is called the generator of the multiresolution analysis.

(In this paper, ' $a \sim b$ ' means that both quantities can be uniformly bounded by some constant multiple of each other. Likewise, ' \lesssim ' will always indicate inequality up to constant factors). The properties (2.2), (2.5), (2.7), and (2.8) immediately imply that φ is *refinable*, i.e., it satisfies a *two-scale relation*

$$\varphi(x) = \sum_{k \in \mathbf{Z}} a_k \varphi(2x - k), \quad (2.9)$$

with the *mask* $\mathbf{a} = \{a_k\}_{k \in \mathbf{Z}} \in \ell_2(\mathbf{Z})$. Because the union of the spaces $\{V_j\}_{j \in \mathbf{Z}}$ is dense in $L_2(\mathbf{R})$, it is easy to see that the construction of a wavelet basis reduces to finding a function whose translates span a complement space W_0 of V_0 in V_1 ,

$$V_1 = V_0 \oplus W_0, \quad W_0 = \overline{\text{span}\{\psi(\cdot - k) \mid k \in \mathbf{Z}\}}. \quad (2.10)$$

Indeed, if we define

$$W_j := \{f(\cdot) \in L_2(\mathbf{R}) \mid f(2^{-j}\cdot) \in W_0\}, \quad (2.11)$$

it follows from (2.3), (2.4) and (2.5) that

$$L_2(\mathbf{R}) = \bigoplus_{j=-\infty}^{\infty} W_j, \quad (2.12)$$

so that

$$\psi_{j,k}(x) = 2^{j/2} \psi(2^j x - k), \quad j, k \in \mathbf{Z} \quad (2.13)$$

forms a wavelet basis of $L_2(\mathbf{R})$.

Obviously, (2.5) and (2.7) imply that the wavelet ψ can be found by means of a functional equation of the form

$$\psi(x) = \sum_{k \in \mathbf{Z}} b_k \varphi(2x - k), \quad (2.14)$$

where the sequence $\mathbf{b} := \{b_k\}_{k \in \mathbf{Z}}$ has to be judiciously chosen; see, e.g., [6, 14, 39] for details.

The construction outlined above is quite general. In many applications, it is convenient to impose some more conditions, i.e., to require that functions on different scales are orthogonal with respect to the usual L_2 -inner product, i.e.,

$$\langle \psi(2^j \cdot -k), \psi(2^{j'} \cdot -k') \rangle = 0, \quad \text{if } j \neq j'. \quad (2.15)$$

This can be achieved if the translates of ψ not only span an (algebraic) complement but the orthogonal complement,

$$V_0 \perp W_0, \quad W_0 = \overline{\text{span}\{\psi(\cdot - k) \mid k \in \mathbf{Z}\}}. \quad (2.16)$$

The resulting functions are sometimes called *pre-wavelets*. The basic properties of refinable functions and (pre-) wavelets can be summarized as follows:

- Reproduction of Polynomials. If φ is contained in

$$C_0^r(\mathbf{R}) := \{g \mid g \in C^r(\mathbf{R}) \text{ and } \text{supp } g \text{ compact}\},$$

then every monomial x^α , $\alpha \leq r$ has an expansion of the form

$$x^\alpha = \sum_{k \in \mathbf{Z}} c_k^\alpha \varphi(x - k). \quad (2.17)$$

- Oscillations. If the generator φ is contained in $C_0^r(\mathbf{R})$, then the associated wavelet ψ has vanishing moments up to order r , i.e.,

$$\int_{\mathbf{R}} x^\alpha \psi(x) dx = 0 \quad \text{for all } 0 \leq \alpha \leq r. \quad (2.18)$$

- Approximation. If $\varphi \in C_0^r(\mathbf{R})$ and f is contained in the usual L_2 -Sobolev space $H^r(\mathbf{R})$, then the following Jackson-type inequality holds:

$$\inf_{g \in V_j} \|f - g\|_{L_2(\mathbf{R})} \lesssim 2^{-jr} |f|_{H^r}. \quad (2.19)$$

(For further information concerning Sobolev as well as other function spaces, the reader is referred to [1]). In practice, it is clearly desirable to work with an *orthonormal* wavelet basis. This can be realized as follows. Given an ℓ_2 -stable generator in the sense of (2.8), one may define another generator ϕ by

$$\hat{\phi}(\xi) := \frac{\hat{\varphi}(\xi)}{(\sum_{k \in \mathbf{Z}} |\hat{\varphi}(\xi + 2\pi k)|^2)^{1/2}}, \quad (2.20)$$

and it can be checked directly that the translates of ϕ are orthonormal and span the same space V_0 . (Clearly, $\hat{\varphi} = \mathcal{F}(\varphi)$ denotes the L_2 -Fourier transform of φ). The generator ϕ is also refinable,

$$\phi(x) = \sum_{k \in \mathbf{Z}} \hat{a}_k \phi(2x - k) \quad \{\hat{a}_k\}_{k \in \mathbf{Z}} \in \ell_2(\mathbf{Z}), \quad (2.21)$$

and it can be shown that the function

$$\psi(x) = \sum_{k \in \mathbf{Z}} (-1)^k \hat{a}_{1-k} \phi(2x - k) \quad (2.22)$$

is an orthonormal wavelet with the same regularity properties as the original generator φ . However, this approach has a serious disadvantage. If the generator φ is compactly supported, this property will in general not carry over to the resulting wavelet since it gets lost during the orthonormalization procedure (2.20). Therefore the compact support will only be preserved if we can dispense with the orthonormalization procedure, i.e., if the translates of φ are already orthonormal. This observation was the starting point for the investigations of I. Daubechies [13, 14] who constructed a family ϕ^N , $N \in \mathbf{N}$ of generators with the following properties.

Theorem 2.1 *There exists a constant $\beta > 0$ and a family ϕ^N of generators satisfying $\phi^N \in C^{\beta N}(\mathbf{R})$, $\text{supp } \phi^N = [0, 2N - 1]$, and*

$$\langle \phi^N(\cdot), \phi^N(\cdot - k) \rangle = \delta_{0,k}, \quad \phi^N(x) = \sum_{k=N_1}^{N_2} a_k \phi^N(2x - k). \quad (2.23)$$

Obviously, (2.23) and (2.22) imply that the associated wavelet ψ^N is also compactly supported with the same regularity properties as ϕ^N .

Given such an orthonormal wavelet basis, any function $f \in V_j$ has two equivalent representations, the *single scale representation* with respect to the functions $\phi_{j,k}(x) := 2^{j/2} \phi(2^j x - k)$ and the *multiscale representation* which is based on the functions $\phi_{0,k}, \psi_{l,m}$, $k, m \in \mathbf{Z}, 0 \leq l < j, \psi_{l,m} = 2^{j/2} \psi(2^j x - m)$. From the coefficients of f in the single scale representation, the coefficients in the multiscale representation can easily be obtained by some kind of filtering, and vice versa. Indeed, given

$$f = \sum_{k \in \mathbf{Z}} \lambda_k^j \phi_{j,k}$$

and using the refinement equation (2.21) and the functional equation (2.22), it turns out that

$$f = \sum_{l \in \mathbf{Z}} 2^{-1/2} \left(\sum_{k \in \mathbf{Z}} \bar{a}_{k-2l} \lambda_k^j \right) \phi_{j-1,l} + \sum_{m \in \mathbf{Z}} 2^{-1/2} \left(\sum_{k \in \mathbf{Z}} \bar{b}_{k-2m} \lambda_k^j \right) \psi_{j-1,m}. \quad (2.24)$$

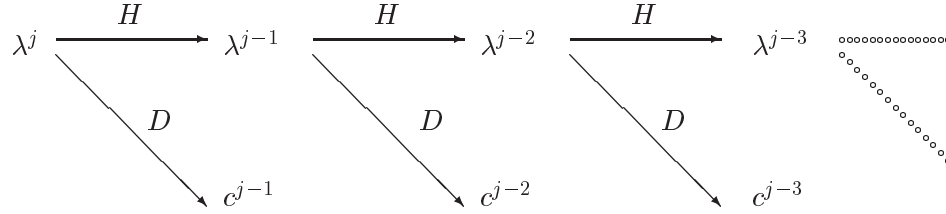
From (2.24) we observe that the coefficient sequence $\lambda^{j-1} = \{\lambda_k^{j-1}\}_{k \in \mathbf{Z}}$ which describes the information corresponding to V_{j-1} can be obtained by applying the low-pass filter H induced by \mathbf{a} to λ^j ,

$$\lambda^{j-1} = H\lambda^j, \quad \lambda_l^{j-1} = \sum_{k \in \mathbf{Z}} 2^{-1/2} \bar{a}_{k-2l} \lambda_k^j. \quad (2.25)$$

The wavelet space W_{j-1} describes the detail information added to V_{j-1} . From (2.24), we can conclude that this information can be obtained by applying the high-pass filter D induced by \mathbf{b} to λ^j :

$$c^{j-1} = D\lambda^j, \quad c_l^{j-1} = 2^{-1/2} \sum_{k \in \mathbf{Z}} \bar{b}_{k-2l} \lambda_k^j. \quad (2.26)$$

By iterating this decomposition method, we obtain a pyramid algorithm, the so-called *fast wavelet transform*:



A reconstruction algorithm can be obtained in a similar fashion. Indeed, a straightforward computation shows

$$\sum_{l \in \mathbf{Z}} \lambda_l^j \phi_{j,l} = \frac{1}{\sqrt{2}} \sum_{l \in \mathbf{Z}} \left(\sum_{k \in \mathbf{Z}} a_{l-2k} \lambda_k^{j-1} + \sum_{n \in \mathbf{Z}} b_{l-2n} c_n^{j-1} \right) \phi_{j,l}$$

so that

$$\lambda_l^j = 2^{-1/2} \sum_{k \in \mathbf{Z}} a_{l-2k} \lambda_k^{j-1} + 2^{-1/2} \sum_{n \in \mathbf{Z}} b_{l-2n} c_n^{j-1}. \quad (2.27)$$

Similar decomposition and reconstruction schemes also exist for the pre-wavelet case.

2.2 Biorthogonal Bases

Given an orthonormal wavelet basis, the basic calculations are usually quite simple. For instance, the wavelet expansion of a function $f \in L_2(\mathbf{R})$ can be computed as

$$f = \sum_{j,k \in \mathbf{Z}} \langle f, \psi_{j,k} \rangle \psi_{j,k}, \quad \psi_{j,k}(x) = 2^{j/2} \psi(2^j x - k). \quad (2.28)$$

However, requiring smoothness and orthonormality is quite restrictive, and consequently, as we have already seen above, the resulting wavelets are usually not compactly supported. It is one of the advantages of the pre-wavelet setting that the compact support property of the generator can be preserved. Moreover, since we have to deal with weaker conditions, the pre-wavelet approach provides us with much more flexibility. Therefore, given a generator φ , many different families of pre-wavelets adapted to a specific application can be constructed. Nevertheless, since

orthonormality is lost, one is still interested in finding suitable alternatives which in some sense provide a compromise between both concepts. This can be performed by using the *biorthogonal* approach. For a given wavelet basis $\{\psi_{j,k}, j, k \in \mathbf{Z}\}$, one is interested in finding a second system $\{\tilde{\psi}_{j,k}, j, k \in \mathbf{Z}\}$ satisfying

$$\langle \psi_{j,k}(\cdot), \tilde{\psi}_{j',k'}(\cdot) \rangle = \delta_{j,j'} \delta_{k,k'}, \quad j, j', k, k' \in \mathbf{Z}. \quad (2.29)$$

Then all the computations are as simple as in the orthonormal case, i.e.,

$$f = \sum_{j,k \in \mathbf{Z}} \langle f, \tilde{\psi}_{j,k} \rangle \psi_{j,k} = \sum_{j',k' \in \mathbf{Z}} \langle f, \psi_{j',k'} \rangle \tilde{\psi}_{j',k'}. \quad (2.30)$$

To construct such a biorthogonal system, one needs *two* sequences of approximation spaces $\{V_j\}_{j \in \mathbf{Z}}$ and $\{\tilde{V}_j\}_{j \in \mathbf{Z}}$. As for the orthonormal case, one has to find bases for certain algebraic complement spaces W_0 and \tilde{W}_0 satisfying the biorthogonality conditions

$$V_0 \perp \tilde{W}_0, \quad \tilde{V}_0 \perp W_0, \quad V_0 \oplus W_0 = V_1, \quad \tilde{V}_0 \oplus \tilde{W}_0 = \tilde{V}_0. \quad (2.31)$$

This is quite easy if the two generators φ and $\tilde{\varphi}$ form a *dual pair*,

$$\langle \varphi(\cdot), \tilde{\varphi}(\cdot - k) \rangle = \delta_{0,k}. \quad (2.32)$$

Indeed, then two biorthogonal wavelets ψ and $\tilde{\psi}$ can be constructed as

$$\psi(x) = \sum_{k \in \mathbf{Z}} (-1)^k d_{1-k} \varphi(2x - k), \quad \tilde{\psi}(x) = \sum_{k \in \mathbf{Z}} (-1)^k a_{1-k} \tilde{\varphi}(2x - k) \quad (2.33)$$

where

$$\varphi(x) = \sum_{k \in \mathbf{Z}} a_k \varphi(2x - k), \quad \tilde{\varphi}(x) = \sum_{k \in \mathbf{Z}} d_k \tilde{\varphi}(2x - k). \quad (2.34)$$

Therefore, given a *primal* generator φ , one has to find a smooth and compactly supported *dual* generator $\tilde{\varphi}$ satisfying (2.32) which is much less restrictive than the orthonormal setting. Elegant constructions can be found, e.g., in [8]. Generalizations to higher dimensions also exist [7]. The basic properties of wavelets and refinable functions (approximation, oscillation etc.) carry over to the biorthogonal setting in the usual way.

For further information on wavelet analysis, the reader is referred to one of the excellent textbooks on wavelets which have appeared quite recently [6, 14, 29, 39, 52].

2.3 Continuous Wavelet Transform

There exists a quite different approach to wavelet analysis which is based on group theory and which yields the so-called *continuous wavelet transform*. Several aspects of radar analysis are closely related with this concept. Hence, we have to discuss some of the basic facts. Continuous wavelet transforms are based on square integrable representations of specific groups. In general, a

unitary irreducible representation \mathcal{U} of a group G in a Hilbert space \mathcal{H} is called *square integrable* if there exists a vector ψ in \mathcal{H} such that

$$\int_G |\langle \psi, \mathcal{U}(g)\psi \rangle|^2 d\mu(g) < \infty, \quad (2.35)$$

where $d\mu$ denotes the invariant Haar measure on G . A vector satisfying (2.35) is called *admissible*. If ψ is admissible, then the mapping

$$\begin{aligned} T_\psi : \mathcal{H} &\rightarrow L_2(G, d\mu) \\ f &\mapsto \langle f, \mathcal{U}(g)\psi \rangle \end{aligned} \quad (2.36)$$

is well-defined, see [24] for details. The 1-D continuous wavelet transform is performed by means of the so-called *affine group* G_A given by

$$G_A : \{(a, b) \mid (a, b) \in \mathbf{R}^2, a \neq 0\} \quad (2.37)$$

with group law

$$(a, b) \circ (a', b') = (aa', ab' + b) \quad (2.38)$$

and (left) invariant Haar measure

$$d\mu = \frac{da db}{a^2}. \quad (2.39)$$

G_A possesses a square integrable representation in $L_2(\mathbf{R})$ given by

$$\mathcal{U}(a, b)f(x) := |a|^{-\frac{1}{2}} f\left(\frac{x-b}{a}\right), \quad (2.40)$$

and every vector $\psi \in L_2(\mathbf{R})$ with

$$\int_{\mathbf{R}} \frac{|\hat{\psi}(\xi)|^2}{|\xi|} d\mu < \infty \quad (2.41)$$

is admissible, see [25] for details. For such a ψ , the *continuous wavelet transform*

$$(W_\psi f)(a, b) := \langle f, \mathcal{U}(a, b)\psi \rangle = \int_{\mathbf{R}} f(x) |a|^{-1/2} \overline{\psi\left(\frac{x-b}{a}\right)} dx \quad (2.42)$$

is well-defined. Moreover, the wavelet transform W_ψ is a multiple of an isometry whose inverse is given by the adjoint wavelet transform

$$F(x) = W_\psi^* (W_\psi F(a, b)) (x) = \frac{1}{C_\psi} \int_{\mathbf{R}} \int_{\mathbf{R} \setminus \{0\}} (W_\psi F)(a, b) |a|^{-1/2} \psi\left(\frac{x-b}{a}\right) \frac{da}{a^2} db, \quad (2.43)$$

see, e.g., [14, 30, 33] for details. The transform (2.42) is sometimes called a *mathematical microscope* since the signal f is analyzed by shifting the microscope ψ according to the different values of b and zooming in by changing the parameter a .

Another important example we shall be concerned with is the famous *Weyl–Heisenberg group*

$$G_{WH} := \{(\omega, b, \tau) \mid b, \omega \in \mathbf{R}, \tau \in \mathbf{C}, |\tau| = 1\} \quad (2.44)$$

with group law

$$(\omega, b, \tau) \circ (\omega', b', \tau') = (\omega + \omega', b + b', \tau\tau' e^{i(\omega b' - \omega' b)/2}). \quad (2.45)$$

The Weyl–Heisenberg group possesses a unitary irreducible representation \tilde{U} in $L_2(\mathbf{R})$ which is given by $\tilde{U}(\omega, b, \tau)f(x) = \tau e^{-i\omega b/2} e^{i\omega x} f(x - b)$. It can be checked that \tilde{U} is square integrable and that every function ψ in $L^2(\mathbf{R})$ is admissible, see [25] for details. If we ignore the total component of the group representation \tilde{U} , i.e., if we define

$$U(\omega, b)f(x) := e^{i\omega x} f(x - b), \quad (2.46)$$

then definition (2.36) leads us to the *windowed Fourier transform*

$$(G_\psi f)(\omega, b) := \int_{\mathbf{R}} f(x) \psi(x - b) e^{-i\omega x} dx. \quad (2.47)$$

The setting of square integrable group representations is closely related with uncertainty principles as we shall now explain. Let $g = (g_1, \dots, g_r)$ be an element of G . Furthermore, let f be a vector belonging to \mathcal{H} . With respect to the representation \mathcal{U} we define *observation operators* (or so-called infinitesimal operators) by

$$[A(g_i)f](x) := \left. \frac{\partial}{\partial g_i} [\mathcal{U}(g)f](x) \right|_{g=e}, \quad (2.48)$$

where e denotes the unit element of G . Let $A = A(g_i) : \mathcal{D}(A) \rightarrow \mathcal{H}$ be some observation operator where $\mathcal{D}(A) \subset \mathcal{H}$ denotes the domain of A . The following definitions are very helpful in the context of uncertainty principles. We define the normalized expectation of A with respect to $h \in \mathcal{D}(A)$ by

$$\mu_h(A) := \frac{\langle Ah, h \rangle}{\|h\|^2} \quad (2.49)$$

and the variance of A with respect to $h \in \mathcal{D}(A)$ by

$$\Delta_h^2(A) := \mu_h((A - \mu_h(A))^2) = \mu_h(A^2) - \mu_h(A)^2. \quad (2.50)$$

The following theorem holds for self-adjoint and non-commuting operators and establishes a very general uncertainty framework, see [49] for details.

Theorem 2.2 Assume that A and B are non-commuting and self-adjoint operators and let the commutator be given by $[A, B] = AB - BA = iC$. Then for all $h \in \mathcal{D}([A, B])$ the following uncertainty relation

$$\mu_h(C)^2 \leq 4\mu_h(A^2)\mu_h(B^2) \quad (2.51)$$

holds. One has equality in (2.51) if and only if there exists a parameter $t \in \mathbf{R}$ with

$$(A - itB)h = 0 \quad \text{or equivalently} \quad (A^2 + t^2B^2)h = -tCh. \quad (2.52)$$

Proof: At first, we compute $(A - itB)^*(A - itB) = A^2 + tC + t^2B^2$. This holds for all $t \in \mathbf{R}$. Hence, for all $h \in \mathcal{D}([A, B])$, with $\|h\| = 1$, we have

$$0 \leq \|(A - itB)h\|^2 = \mu_h(A^2) + t\mu_h(C) + t^2\mu_h(B^2), \quad (2.53)$$

which is a real and nonnegative parabola in t . Consequently, the condition

$$D = \left(\frac{\mu_h(C)}{2\mu_h(B^2)} \right)^2 - \frac{\mu_h(A^2)}{\mu_h(B^2)} \leq 0 \quad (2.54)$$

is fulfilled. This proves inequality (2.51). One has equality in (2.51) if there exists a $t \in \mathbf{R}$ with $D = 0$ (a root of second order). This is equivalent to the eigenvalue problem $(A - itB)h = 0$ or to $(A - itB)^*(A - itB)h = 0$. \square

2.4 Frames

In the previous sections, we were concerned with function systems that form some kind of (or-thonormal) basis for $L_2(\mathbf{R})$. This is clearly very convenient, however, for technical reasons, this requirement is sometimes too restrictive in radar applications. We refer to Section 5 for further information. Therefore we shall now discuss a weaker concept which is given by the frame approach. Then every function in $L_2(\mathbf{R})$ can be written in terms of the frame elements, but the expansions may contain some redundancy.

In general, a system $\{h_m\}_{m \in \mathbf{Z}}$ of functions is called a *frame* if there exist constants \tilde{A} and \tilde{B} , $0 < \tilde{A} \leq \tilde{B} < \infty$, such that

$$\tilde{A}\|F\|_{L_2(\mathbf{R})}^2 \leq \sum_{m \in \mathbf{Z}} |\langle F, h_m \rangle|^2 \leq \tilde{B}\|F\|_{L_2(\mathbf{R})}^2. \quad (2.55)$$

The numbers \tilde{A}, \tilde{B} are called *frame bounds*. Given a frame $\{h_m\}_{m \in \mathbf{Z}}$, one defines the *frame operator* T as

$$T(F) := \sum_{m \in \mathbf{Z}} \langle F, h_m \rangle h_m. \quad (2.56)$$

For later use, let us recall the following fundamental theorem which was proved in [16].

Theorem 2.3 Let $\{h_m\}_{m \in \mathbf{Z}}$ be a frame in $L_2(\mathbf{R})$. Then the following holds.

- i) T is invertible and $\tilde{B}^{-1}I \leq T^{-1} \leq \tilde{A}^{-1}I$.
- ii) $\{h^m\}_{m \in \mathbf{Z}}$, $h^m := T^{-1}h_m$ is a frame with bounds \tilde{A}^{-1} , \tilde{B}^{-1} , called the dual frame of $\{h_m\}_{m \in \mathbf{Z}}$.
- iii) Every $F \in L_2(\mathbf{R})$ can be written as

$$F = \sum_{m \in \mathbf{Z}} \langle F, h^m \rangle h_m = \sum_{m \in \mathbf{Z}} \langle F, h_m \rangle h^m. \quad (2.57)$$

Furthermore, we need a result concerning the Fourier transform of frames.

Lemma 2.1 *Let $\{h_m\}_{m \in \mathbf{Z}}$ be a frame and let $\{h^m\}_{m \in \mathbf{Z}}$ denote the dual frame. Then the set $\{\hat{h}_m\}_{m \in \mathbf{Z}}$ also constitutes a frame and the dual frame is defined by $(\hat{h})^m = \frac{1}{(2\pi)} \widehat{h^m}$.*

3 Statistical Curve Estimation Using Wavelets

In Section 2.1 we discussed techniques to express f by means of a wavelet basis. Such a wavelet expansion is a special kind of orthogonal series estimator. Unlike traditional Fourier bases, wavelet bases offer a degree of localization in space as well as in the frequency domain. This enables us to develop simple function estimates that respond effectively to discontinuities and spatially varying degrees of oscillations in a signal, even when the observation are contaminated by noise.

In this section, we consider the problem of nonparametric regression estimation of a function f by wavelet methods. The *regression model* is given by

$$Y_i = f(X_i) + \xi_i, \quad i = 1, \dots, n, \quad (3.1)$$

where ξ_i are i.i.d., $E(\xi_i) = 0$ and X_i are equidistant points in the interval $[0, 1]$: $X_i = i/n$. The effect of nonlinear smoothing will become visible in our radar application. The nonlinearity, introduced through thresholding of wavelet coefficients, guarantees smoothness adaptivity of the estimators.

3.1 Threshold Wavelet Estimator

A natural *linear estimator* of f can be constructed by estimating projection the $P_{j_0}f$ on V_{j_0} and is defined as

$$f_n = \bar{P}_{j_0}f = \sum_k \bar{\lambda}_k^{j_1} \phi_{j_1 k} + \sum_{j=j_1}^{j_0} \sum_k \bar{\gamma}_k^j \psi_{j k}, \quad (3.2)$$

with empirical coefficients λ_k^j, γ_k^j given by

$$\bar{\lambda}_k^j = \frac{1}{n} \sum_{i=1}^n Y_i \phi_{j k}(X_i) \quad \text{and} \quad \bar{\gamma}_k^j = \frac{1}{n} \sum_{i=1}^n Y_i \psi_{j k}(X_i). \quad (3.3)$$

This choice of $\bar{\lambda}_k^j$ and $\bar{\gamma}_k^j$ is motivated by the fact that (3.3) are ‘almost’ unbiased estimators for large n . We are interested in the worst case performance of our estimator over a variety of function spaces, for further details see [18, 19]:

$$R(f_n, \mathcal{F}) = \sup_{f \in \mathcal{F}} E \|f_n - f\|_{p'}^{p'}. \quad (3.4)$$

For our purpose we choose as function spaces under consideration the so-called Besov spaces which can be introduced as follows.

The modulus of smoothness $\omega_r(f, t)_{L_p(\mathbf{R})}$ of a function $f \in L_p(\mathbf{R})$, $0 < p \leq \infty$, is defined by

$$\omega_r(f, t)_{L_p(\mathbf{R})} := \sup_{|h| \leq t} \|\Delta_h^r(f, \cdot)\|_{L_p(\mathbf{R})}, \quad t > 0,$$

with Δ_h^r the r -th difference with step h . For $\alpha > 0$ and $0 < q, p \leq \infty$, the Besov space $B_q^\alpha(L_p(\mathbf{R}))$ is defined as the space of all functions f for which

$$|f|_{B_q^\alpha(L_p(\mathbf{R}))} := \begin{cases} \left(\int_0^\infty [t^{-\alpha} \omega_r(f, t)_{L_p(\mathbf{R})}]^q dt/t \right)^{1/q}, & 0 < q < \infty, \\ \sup_{t \geq 0} t^{-\alpha} \omega_r(f, t)_{L_p(\mathbf{R})}, & q = \infty, \end{cases} \quad (3.5)$$

is finite with $r := [\alpha] + 1$. Then, (3.5) is a (quasi-)semi-norm for $B_q^\alpha(L_p(\mathbf{R}))$. If we add $\|f\|_{L_p(\mathbf{R})}$ to (3.5), we obtain a (quasi-)norm for $B_q^\alpha(L_p(\mathbf{R}))$.

Remark 3.1 *It is well-known that for $p = q = 2$ Sobolev and Besov spaces coincide,*

$$H^\alpha(\mathbf{R}) = B_2^\alpha(L_2(\mathbf{R})), \quad (3.6)$$

see again [1] for details.

In our setting the spaces of interest are defined by

$$\mathcal{F}_p^\alpha(M) := \{f \in B_p^\alpha(L_p(\mathbf{R})) : \|f\|_{B_p^\alpha(L_p(\mathbf{R}))} \leq M\}, \quad (3.7)$$

where α and $p = q$ are known parameters. Moreover, as in [18] we extend the linear to the non-linear setting. Among all non-linear estimators, we choose a very special one: the *truncated co-ordinatewise hard threshold wavelet estimator* which is given by

$$f_n^* = \sum_k \bar{\lambda}_k^{j_1} \phi_{j_1 k} + \sum_{j=j_1}^{j_0} \sum_k \theta_h(\bar{\gamma}_k^j, t) \psi_{jk}, \quad (3.8)$$

where

$$\theta_h(\bar{\gamma}_k^j, t) = \bar{\gamma}_k^j \cdot 1\{|\bar{\gamma}_k^j| > t\}, \quad t = KC(j)n^{-1/2}, \quad (3.9)$$

and $C(j)$ has to be appropriately chosen, see Theorem 3.1 below for details.

3.2 Error Bounds

This section is concerned with the behavior of (3.8), for details see [18]. To keep the notation at a reasonable level, we introduce the following variables

$$\begin{aligned}\alpha' &= \alpha - 1/p + 1/p', \\ \delta &= \min(\alpha/(2\alpha + 1), \alpha'/(1 + 2\alpha - 2/p)) \quad \text{and} \\ \epsilon &= \alpha p - (p' - p)/2.\end{aligned}$$

The notation $2^{j(n)} \simeq g(n)$ means that $2^{j(n)}$ is chosen to satisfy the inequalities $2^{j(n)} \leq g(n) \leq 2^{j(n+1)}$.

Theorem 3.1 *Let $p' \geq p \vee 1$, $\alpha - 1/p > 0$ and suppose that f belongs to*

$$\mathcal{F}_p^\alpha(M, T) = \{f \in \mathcal{F}_p^\alpha(M) : \text{supp} f \subset [-T, T]\}.$$

If $C(j) = \sqrt{j}$, there exist constants $C = C(\alpha, p, M)$ and K_0 such that if

$$\begin{aligned}2^{j_1(n)} &\simeq \left(n (\log n)^{\frac{p'-p}{p} 1_{\{\epsilon \geq 0\}}} \right)^{1-2\delta} \\ 2^{j_0(n)} &\simeq \left(n (\log n)^{-1_{\{\epsilon \leq 0\}}} \right)^{\delta/\alpha'}\end{aligned}$$

and $K \geq K_0$, then

$$\sup_{f \in \mathcal{F}_p^\alpha(M, T)} E \|f_n^* - f\|_{p'}^{p'} \leq \begin{cases} C (\log n)^{(1-\epsilon/\alpha p)\delta p'} n^{-\delta p'} & \epsilon > 0 \\ C (\log n)^{\max(p'/2-1, 0)} \left(\frac{\log n}{n}\right)^{\delta p'} & \epsilon = 0 \\ C \left(\frac{\log n}{n}\right)^{\delta p'} & \epsilon < 0. \end{cases} \quad (3.10)$$

For comprehensive remarks and a proof of Theorem 3.1 we refer the reader to [18]. However, as is well known in practice, for many applications the observations can no longer be assumed to come from a stationary error. A more generalized model based on a time series setting with locally stationary errors was discussed in [47]. Then, for the case $p' = 2$ one obtains the ‘classical’ rate for the L_2 -risk by exactly the same treatment of the empirical coefficients as in the white noise case. This rate is attained for the optimal threshold (not known in practice, however) whereas a data-driven threshold that comes quite close is, e.g.

$$t_{jk} = \bar{\sigma}_{jk} \sqrt{2 \log(\#\mathcal{I}_n)}, \quad (3.11)$$

where $\mathcal{I}_n = \{(j, k) : 2^j \leq Cn^{1-\epsilon}\}$ for some $\epsilon > 0$, e.g. $\epsilon \leq 1/3$.

4 Basic Radar Setting

This section is concerned with the introduction and discussion of basic radar models. We derive two models, the wideband and narrowband model. In radar signal processing one important question is how to choose the optimal waveform. Theoretically, this question is related to the choice

of the analyzing wave function. In Section 4.3, we show that there is a notable relation with uncertainty principles. Moreover, it is known that the narrowband approach is the most suitable one for many applications. For that reason and with regard to our meteorological radar application we show in Section 4.4 how one can discretize the narrowband model. Later on this discretized model will be the basis for meteorological radar signal processing.

4.1 Wideband Model

Suppose we want to find the location and velocity of an object, such as an airplane. One way to achieve this is to send out an electromagnetic wave in the direction of the object and observe the echo that is reflected to the source. As we shall now explain, a comparison between the outgoing signal and its echo allows an approximate determination of the distance R of the object and the radial velocity v along the line-of-sight. This is the problem of radar in its most elementary form. For a thorough treatment, we refer to the classical books of Cook and Bernfeld [9], Rihaczek [45] and Woodward [55]. The wavelet-based analysis has been initiated by Naparst [40, 41]. In this paper, our major reference will always be the book of Kaiser [30].

To explain the basic radar setting, let us first assume that the object under consideration can be described as a single point. The outgoing signal is modeled as a real-valued function of time, i.e., $h : \mathbf{R} \rightarrow \mathbf{R}$, representing the voltage fed into a transmitting antenna. The antenna transmits $h(t)$ into an electromagnetic wave and beams it into the desired direction. We assume that the returning echo, also a full electromagnetic wave, is converted by the same device to a real function $f(t)$, which again represents a voltage.

The objective is to predict the trajectory of the point object. If at time $t = 0$ the object is located at R_0 and if it is moving with speed v , then its trajectory is given by

$$R(t) = R_0 + vt. \quad (4.1)$$

Consequently, the task is to determine R_0 and v from f . To this end, we proceed as follows. According to (4.1), at time t , the moving point object is at a position $R_0 + vt$, i.e., at this instant it reflects a signal which was sent out at time

$$t - \frac{R_0 + vt}{c},$$

where we have simply used the fact that electromagnetic waves propagate with the speed of light $c \approx 3 \times 10^8$ m/sec. In other words, the object reflects the signal

$$s(t) = ah \left(t - \frac{R_0 + vt}{c} \right),$$

where a is a factor which describes the reflectivity of the object. This signal then produces an echo which is time-delayed by $(R_0 + vt)/c$,

$$f \left(t + \frac{R_0 + vt}{c} \right) = s(t) = ah \left(t - \frac{R_0 + vt}{c} \right),$$

or what is the same thing

$$f\left(t + \frac{R_0}{c}\right) = ah\left(\left(t - \frac{R_0}{c}\right)\left(\frac{c-v}{c+v}\right) - \frac{R_0}{c}\right).$$

Consequently, by introducing the new coordinates

$$s_0 = \frac{c+v}{c-v}, \quad \tau_0 = \frac{2R_0}{c-v}, \quad (4.2)$$

we obtain the basic relation

$$f(t) = ah\left(\frac{t - \tau_0}{s_0}\right). \quad (4.3)$$

The whole situation is visualized in Figure 1 below. We see that the incident wave is scaled by the factor s_0 , this is nothing else but the well-known Doppler effect. Therefore the new coordinates s_0 and τ_0 are sometimes called *Doppler coordinates*. All material objects move with speeds less than c , hence $s_0 > 0$ always. If $v > 0$, i.e., the object is moving away, then f is a stretched version of ψ . Similarly, when $v < 0$, the reflected signal is a compressed version of h . The value of a clearly depends on the amount of amplification performed on the echo. In the sequel, we shall always assume that $a = s_0^{-1/2}$, so that f has the same energy as h , i.e., $\|f\|^2 = \|h\|^2$. From (4.2), it is clear that v and R_0 can be obtained from s_0 and τ_0 , i.e.,

$$v = \frac{s_0 - 1}{s_0 + 1}c, \quad R_0 = \frac{c\tau_0}{s_0 + 1}. \quad (4.4)$$

Therefore, to compute v and R_0 , it is sufficient to determine s_0 and τ_0 . This is done by considering the whole family of scaled and translated versions of h :

$$\{h_{s,\tau} : s > 0, \tau \in \mathbf{R}\}, \quad h_{s,\tau} = s^{-1/2}h\left(\frac{t - \tau}{s}\right). \quad (4.5)$$

We regard $h_{s,\tau}$ as a test signal which is compared with f , i.e., a given return f is matched with $h_{s,\tau}$ by taking inner product,

$$\tilde{f}(s, \tau) = \int_{-\infty}^{\infty} f(t)s^{-1/2}h\left(\frac{t - \tau}{s}\right) dt. \quad (4.6)$$

$\tilde{f}(s, \tau)$ is called the *wideband cross-ambiguity function* of f . If we compare (4.6) with (2.42), we see that \tilde{f} is nothing else but the continuous wavelet transform of the received echo f . Now (4.3) clearly implies that

$$\tilde{f}(s, \tau) = \langle h_{s,\tau}, h_{s_0,\tau_0} \rangle = \langle \mathcal{U}(s, \tau)h, \mathcal{U}(s_0, \tau_0)h \rangle = R(s, \tau, s_0, \tau_0). \quad (4.7)$$

The *reproducing kernel* R is the *wideband self-ambiguity function* of h . By the Schwartz inequality we have that

$$|\tilde{f}(s, \tau)| \leq \|h_{s,\tau}\| \|h_{s_0,\tau_0}\| = \|h\|^2, \quad (4.8)$$

with equality if $s = s_0, \tau = \tau_0$. Thus, all we have to do is to compute the maxima of the continuous wavelet transform of the received echo!

However, this approach may fail for various reasons. The reflecting object may not be rigid, with different parts having different velocities (consider a cloud). Or, there may be many reflecting objects, each with its own range and velocity. We will model all such situations by assuming that there is a *distribution* of reflectors, described by a *reflectivity density* $D(s, \tau)$. Then the total echo is given by:

$$f(t) = \int_{\mathbf{R}} \int_{\mathbf{R} \setminus \{0\}} D(\tau, s) |s|^{-1/2} h\left(\frac{t - \tau}{s}\right) \frac{ds d\tau}{s^2}. \quad (4.9)$$

Consequently, the task is to reconstruct the density $D(\tau, s)$. This is the *inverse problem* to be solved: knowing h and f , find D . To treat this problem, let us first remark that formula (4.9) can be reinterpreted in the context of wavelet analysis. Indeed, a comparison of (2.43) with (4.9) yields the well-known and basic identity which links wideband radar echoes to wavelet analysis, see e.g. [20, 41, 40]: the echo f is identical with the inverse wavelet transform of the searched reflectivity distribution D where the transmitted signal h plays the role of the analyzing wavelet.

This suggests to recover D by computing the wavelet transform of the echo f :

$$D(\tau, s) := \frac{1}{C_h} [(W_h f)(\tau, s)]. \quad (4.10)$$

However, the null space \mathcal{N} of an inverse wavelet transform is non trivial. Hence by this procedure one can only recover the component of D which lies in the orthogonal complement of \mathcal{N} or equivalently one can recover the component of D in the range of the wavelet transform W_h . To our knowledge, there exists no physical principle that guarantees that D is in fact contained in the range of W_h , so that (4.10) only describes one part of the desired density D . Therefore the general solution reads as follows.

Theorem 4.1 *The most general solution $D(s, \tau)$ in $L_2(ds d\tau / s^2)$ is given by*

$$D(s, \tau) = \tilde{f}(s, \tau) + D(s, \tau)^\perp,$$

where $D(s, \tau)^\perp$ is any function in $\text{rg}(W_h)^\perp$, i.e.,

$$\int \int R(s, \tau, s_0, \tau_0) D(s, \tau)^\perp \frac{ds d\tau}{s^2} = 0.$$

Inspired by these problems, Naparst [40, 41] was the first one who suggested not to transmit just *one* signal but a *family* of signals. In his fundamental work, Naparst primarily studied the case that the transmitted signals form an orthonormal basis. However, this assumption is very restrictive in practice. Therefore, quite recently, Rebollo–Neira, Platino and Fernandez–Rubio generalized Naparst’s approach to the case of transmitting a *frame* of signals, which is a much weaker restriction, see [44]. Further results including error estimates and generalizations to the multivariate case can also be found in [10, 11]. We shall discuss these ideas in Section 5.

4.2 Narrowband Model

The wideband model, which describes echoes for arbitrary signals h , can be simplified for most real-life situations. The commonly used narrowband approximation deals with signals of the form

$$h(t) = e^{-i\omega_c t} \eta(t),$$

where the carrier frequency ω_c is assumed to be much larger than the comparatively narrowbanded frequencies of the modulation function η .

Furthermore, most objects of interest in radar travel with a speed much smaller than light. Thus $|v|/c \ll 1$ and

$$\tau \sim \frac{2R_0}{c}. \quad (4.11)$$

Now we have to treat the positive and negative frequencies of η separately

$$\hat{\eta}_P(\omega) := \hat{\eta}(\omega)\chi_{[0,\infty)}(\omega), \quad \hat{\eta}_R(\omega) := \hat{\eta}(\omega)\chi_{(-\infty,0]}(\omega). \quad (4.12)$$

Removing the carrier frequency ω_c from both, the signal η and the echo f , and neglecting time independent scale factors leads to the standard narrowband model for the echo f of a single moving object

$$f(t) = c \left\{ \eta_P(t - \tau)e^{-i\phi t} + \eta_R(t - \tau)e^{+i\phi t} \right\},$$

where $\phi = 2\omega_c v/c$, see e.g. the classical textbooks [45, 51] and [30] for details. The variables (τ, ϕ) are called the *narrowband Doppler coordinates*.

Consequently, the narrowband model for the echo produced by a reflectivity density $D_{NB}(\phi, \tau)$ is given by

$$f(t) = \int_{\mathbf{R}} \int_{\mathbf{R}} \left\{ \eta_P(t - \tau)e^{-i\phi t} + \eta_R(t - \tau)e^{+i\phi t} \right\} D_{NB}(\phi, \tau) d\phi d\tau. \quad (4.13)$$

We may decompose the space $L_2(\mathbf{R})$ as

$$L_2(\mathbf{R}) \simeq L_{2,P}(\mathbf{R}) \oplus L_{2,R}(\mathbf{R}) \quad (4.14)$$

where

$$L_{2,P}(\mathbf{R}) := \{f \in L_2(\mathbf{R}) \mid \text{supp } \hat{f} \subset [0, \infty), \text{ i.e., } \hat{f}_P = \hat{f}\}, \quad (4.15)$$

$$L_{2,R}(\mathbf{R}) := \{f \in L_2(\mathbf{R}), \mid \hat{f}_R = \hat{f}\}. \quad (4.16)$$

Then the goal is clearly to reconstruct the density $D_{NB}(\phi, \tau)$ from the received echoes. It turns out that a suitable reconstruction formula can indeed be derived, provided that the families of outgoing signals form frames in the spaces $L_{2,P}(\mathbf{R})$ and $L_{2,R}(\mathbf{R})$, respectively, see Subsection 5.4 for details.

The ambiguity function in the narrowband regime can be formulated as follows. As in the wideband case, a general echo is modeled by assuming a distribution of reflectors, now described as a function of the delay and Doppler shifts

$$f(t) = \int \int \Psi_{\phi, \tau}(t) D_{NB}(\phi, \tau) d\phi d\tau, \quad (4.17)$$

where $\Psi_{\phi, \tau}(t) = e^{i\phi t} \Psi(t - \tau)$. Equation (4.17) also poses an inverse problem: given f , find D_{NB} . Just as wavelet analysis was used to analyze and to solve the wideband inverse problem, so can time-frequency analysis be used to do the same for the narrowband problem. This can be seen by recalling the windowed Fourier transform of f with respect to the window function Ψ :

$$\tilde{f}(\phi, \tau) = \int f(t) \bar{\Psi}(t - \tau) e^{-i\phi t} dt. \quad (4.18)$$

Indeed, by comparing (4.17) and (4.18) we can state a version of Theorem 4.1 for the narrowband case.

Theorem 4.2 *The most general solution $D_{NB}(\phi, \tau)$ in $L_2(d\phi d\tau)$ is given by*

$$D_{NB}(\phi, \tau) = \tilde{f}(\phi, \tau) + D_{NB}(\phi, \tau)^\perp,$$

where $D_{NB}(\phi, \tau)^\perp$ is any function in the orthogonal complement of the range of the windowed Fourier transform, i.e.,

$$\int \int R(\phi, \tau, \phi_0, \tau_0) D_{NB}(\phi, \tau)^\perp d\phi d\tau = 0.$$

A reconstruction formula of D_{NB} is presented in Subsection 5.4.

4.3 Localization and Radar Uncertainty Principles

As explained in the Sections 4.1 and 4.2, we can relate the wideband model to the wavelet transform and the narrowband model to the windowed Fourier transform. The fundamental fact is that from the group theoretical point of view, see Section 2.3, there is no essential difference between the wideband and the narrowband treatment. This can be very useful in order to extend our radar models, e.g. to space-time \mathbf{R}^4 , cf. [30]. But a more important concern is that based on the theory of groups we have for both, the wideband and the narrowband model, a uniform setting to establish uncertainty principles, see Theorem 2.2.

To expose the relevance of uncertainty relations in radar modeling we can elaborate on ‘radar imaging’, i.e., recognition and identification of moving objects. In this field one has to focus on localization properties of the analyzing wave function. In [3] this problem was analyzed in the narrowband framework. As a main result it turned out that the optimal wave function in terms of pulsewidth and bandwidth has to minimize a so-called ‘narrowband uncertainty principle’. This

principle coincides with the well-known Heisenberg uncertainty relation, which corresponds to Theorem 2.2 applied to the Weyl-Heisenberg group. This straightforward coherence enables us to compute ‘wideband uncertainty relations’. We only have to exchange the underlying group, i.e., we have to switch to wideband Doppler coordinates (s, τ) introduced in (4.2) which correspond to the affine group, see (2.37), and we have to apply Theorem 2.2.

In general, by the fact that Theorem 2.2 does not depend on the special choice of the group it establishes a very general radar uncertainty framework. Once we have derived a minimizing wave function h with respect to the radar uncertainty, we know that the corresponding generalized self-ambiguity function, compare with (4.7),

$$R(g, g') = \langle \mathcal{U}(g)h, \mathcal{U}(g')h \rangle ,$$

has fast decay in the parameter plane, e.g. time – Doppler scale plane. This corresponds to high resolution properties which is a main goal in radar device design.

As already stated, the narrowband uncertainty principle was extensively studied in [3]. For completeness we give a brief sketch for the wideband uncertainty principle. Let the underlying group be the affine group

$$G_A : \{(s, \tau) | (s, \tau) \in \mathbf{R}^2, s \neq 0\} \quad \text{with group law} \quad (2.38)$$

and let $\mathcal{H} = L_2(\mathbf{R})$. Then, by (2.40) and (2.48) we can derive the observation operators

$$\tilde{A}_s h(x) = \frac{\partial}{\partial s} \mathcal{U}(s, \tau) h(x) |_{(s=1, \tau=0)} = -h(x)/2 - xh'(x) \quad (4.19)$$

$$\tilde{A}_\tau h(x) = \frac{\partial}{\partial \tau} \mathcal{U}(s, \tau) h(x) |_{(s=1, \tau=0)} = -h'(x) . \quad (4.20)$$

By a multiplication with i we obtain self-adjoint operators, i.e. $A_s := i\tilde{A}_s$ and $A_\tau := i\tilde{A}_\tau$. The commutator is given by $[A_s, A_\tau] = -iA_\tau$. Applying Theorem 2.2, we can express the searched uncertainty relation as

$$\mu_h(A_\tau) \leq 4\Delta_h^2(A_s)\Delta_h^2(A_\tau) ,$$

see inequality (2.51). Finally, we have to compute the variance terms explicitly

$$\Delta_h^2(A_\tau) = \|h'\|_2^2 - \mu_h^2(A_\tau) \quad \text{and} \quad \Delta_h^2(A_s) = \|xh'\|_2^2 - \|h\|_2^2/4 - \mu_h^2(A_s) .$$

For comprehensive discussions and computations of uncertainty principles we refer the reader to [12, 49].

4.4 Discrete Narrowband Model

The analysis of many practical applications, e.g. in meteorological radar data processing, is limited by the available bandwidth. In those cases one is not able to reconstruct the reflectivity density

completely. However, to compute the radial velocity one can derive the Doppler frequency of the reflected echo f along the beam direction by estimating the first moment in the Fourier power spectrum.

The radar devices sample the backscattered electromagnetic signals discretely in time. Hence, it is of importance to describe how to discretize the continuously given echo f to obtain a discrete time series. A basic assumption in this setting is that our reflectivity density is now a function depending on ϕ , τ and time t . Furthermore, to create time series corresponding to different heights we assume that our transmitted signal h is a pulse train, i.e. a sum of ΔT time shifted pulses

$$h(t) = e^{iw_c t} \eta(t), \quad \text{with} \quad \eta(t) = \sum_{k=0}^{2^N-1} \mu(t - k\Delta T), \quad (4.21)$$

where μ is a single pulse, e.g. a characteristic function of an interval which is contained in $[0, \Delta T]$. Consequently, we can extend the narrowband model (4.13) to

$$\begin{aligned} f(t) &= \int_{\mathbf{R}} \int_{\mathbf{R}} \left\{ \eta_P(t - \tau) e^{-i\phi t} + \eta_R(t - \tau) e^{+i\phi t} \right\} D_{NB}(t, \phi, \tau) d\phi d\tau \\ &= \int_{\mathbf{R}} \int_{\mathbf{R}} \left\{ \sum_{k=0}^{2^N-1} \mu_P(t - k\Delta T - \tau) e^{-i\phi t} + \sum_{k=0}^{2^N-1} \mu_R(t - k\Delta T - \tau) e^{+i\phi t} \right\} D_{NB}(t, \phi, \tau) d\phi d\tau \\ &= \sum_{k=0}^{2^N-1} \int_{\mathbf{R}} \left\{ \mu_P(t - k\Delta T - \tau) D_{NB}(t, \cdot, \tau)^\wedge(t) + \mu_R(t - k\Delta T - \tau) D_{NB}(t, \cdot, \tau)^\wedge(-t) \right\} d\tau \\ &= \sum_{k=0}^{2^N-1} \int_{\mathbf{R}} \left\{ \mu_P(t - k\Delta T - \tau) D_P(t, \tau) + \mu_R(t - k\Delta T - \tau) D_R(t, \tau) \right\} d\tau \\ &= \sum_{k=0}^{2^N-1} \left\{ \mu_P * D_P(t, \cdot)(t - k\Delta T) + \mu_R * D_R(t, \cdot)(t - k\Delta T) \right\}, \end{aligned}$$

where $D_P(t, \tau) = D_{NB}(t, \cdot, \tau)^\wedge(t)$ and $D_R(t, \tau) = D_{NB}(t, \cdot, \tau)^\wedge(-t)$. Now, we want to sample the complex-valued function f such that we obtain measurements at certain heights. Let the sample frequency be given by $1/\Delta t$ and let us choose a number M such that $\Delta T = M \cdot \Delta t$, see Figure 1. Hence, we obtain values of f at the discrete grid

$$t_0 + m \cdot \Delta t + n \cdot \Delta T \quad \text{with} \quad m = 1, \dots, M \text{ and } n = 0, \dots, 2^N - 1,$$

where the sample sequence is given by

$$f[m, n] = f(t_0 + m \cdot \Delta t + n \cdot \Delta T).$$

To obtain a time series for height $h = c \cdot m_h \cdot \Delta t/2$ we have to fix $m = m_h$

$$f_h = f_h[n] = f[m_h, n] = f(m_h \cdot \Delta t + n \cdot \Delta T),$$

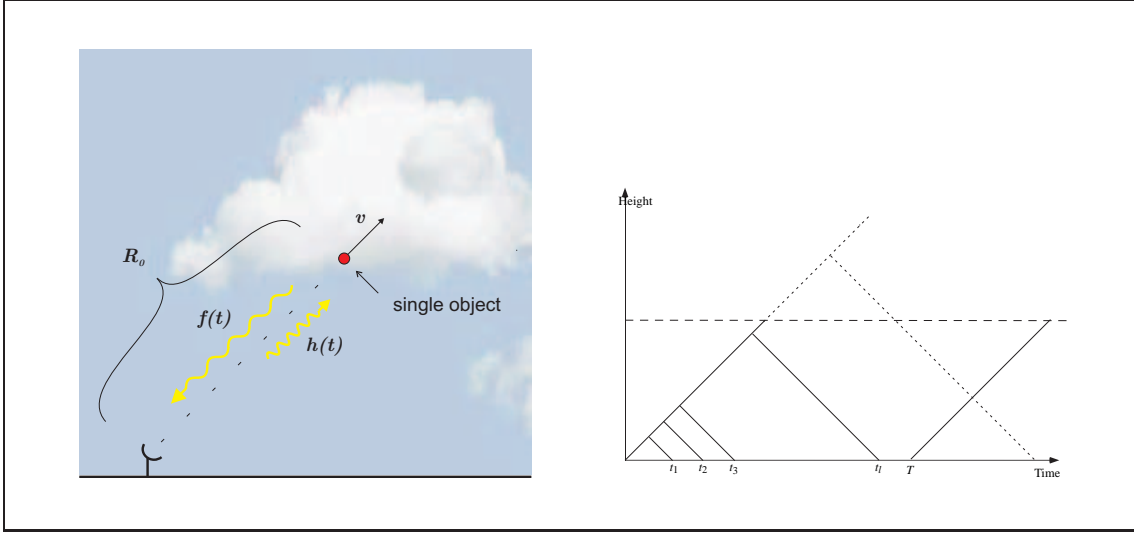


Figure 1: Left: single point model. Right: sampling scheme with respect to time and height.

assuming that $t_0 = 0$. Thus, we obtain for every height a time series of length 2^N . We remark that the radar device measures real-valued voltages only. They are often expressed in terms of circular functions

$$r(t) = a(t) \cos(\omega_c t + \omega(t)) = \Re [f(t)e^{i\omega_c t}] \quad (4.22)$$

where $f(t)$ is the complex envelope, $\omega(t)$ the phase and $a(t)$ the amplitude of the received narrowband signal. It can be assumed that f can be expressed by

$$f(t) = [r(t) + iHr(t)] e^{-i\omega_c t} = I(t) + iQ(t), \quad (4.23)$$

where H denotes the Hilbert transform, see [34] for details. However, the Hilbert transform is not easily implemented in real systems. Instead, the real and imaginary part of the complex envelope f are determined using a quadrature demodulator. Moreover, by low-pass filtering we obtain a modified description of the discretized echo

$$\tilde{I}(t) = 2 [f(t) \cos(\omega_c t)]_{\Theta} \quad \text{and} \quad \tilde{Q}(t) = 2 [f(t) \sin(\omega_c t)]_{\Theta}, \quad (4.24)$$

where Θ denotes the low-pass filter function. Note, that this method is easier implemented either analog or digitally. Finally, this leads to the classical notation of discrete wind profiler radar data at height h

$$\tilde{f}_h[n] = \tilde{I}[n] + i\tilde{Q}[n]. \quad (4.25)$$

5 Analysis of Continuous Reflectivity Densities

In Section 4, we have already discussed the basic radar setting. It has turned out that a dense target environment is described by a certain reflectivity density $D(s, \tau)$. We have also seen that this

density cannot be reconstructed by simply transmitting just one signal. Nevertheless, in the next sections we shall show that a complete reconstruction is possible if we transmit a certain family of signals.

5.1 Basic Reconstruction Formulas in the Wideband Regime

In this subsection, we shall derive a basic reconstruction formula for the wideband setting which guarantees that a given reflectivity density can indeed be reconstructed, provided that the set of outgoing signals forms a frame, compare with Subsection 2.4.

Theorem 5.1 *Let $\{h_m\}_{m \in \mathbf{Z}}$ be a frame of outgoing signals in $L_2(\mathbf{R})$ and let f_m denote the corresponding echoes produced by a reflectivity density $D(\tau, s)$,*

$$f_m(t) = \int_{\mathbf{R}} \int_{\mathbf{R} \setminus \{0\}} D(\tau, s) |s|^{-1/2} h_m \left(\frac{t - \tau}{s} \right) \frac{ds d\tau}{s^2}. \quad (5.1)$$

Let us assume that the following conditions are satisfied

$$D(\tau, s) |s|^{-1/2} h_m \left(\frac{t - \tau}{s} \right) \in L_1 \left(\frac{ds dt d\tau}{s^2} \right), \widehat{D(\cdot, s)}(\omega) \in L_1(d\omega), \widehat{D(\cdot, \sigma)}(\omega) |\sigma|^{-3/2} \in L_2(d\sigma). \quad (5.2)$$

Then $D(\tau, s)$ can be reconstructed as follows

$$\begin{aligned} D(\tau, s) &= \frac{1}{(2\pi)^2} \sum_{m \in \mathbf{Z}} \int_{-\infty}^0 -\frac{1}{i} \widehat{f'_m}(\omega) \widehat{h^m \left(\frac{\cdot}{s} \right)}(\omega) |s|^{1/2} e^{i\tau\omega} d\omega \\ &\quad + \frac{1}{(2\pi)^2} \sum_{m \in \mathbf{Z}} \int_0^{\infty} \frac{1}{i} \widehat{f'_m}(\omega) \widehat{h^m \left(\frac{\cdot}{s} \right)}(\omega) |s|^{1/2} e^{i\tau\omega} d\omega, \end{aligned} \quad (5.3)$$

where $\{h^m\}_{m \in \mathbf{Z}}$ denotes the dual frame of $\{h_m\}_{m \in \mathbf{Z}}$.

Proof: A detailed proof can be found in [10], therefore we only sketch the basic ideas. We first observe that

$$|s|^{-1/2} h_m \left(\frac{\cdot - \tau}{s} \right) (\omega) = |s|^{1/2} e^{-i\omega\tau} \widehat{h}_m(\omega s). \quad (5.4)$$

Therefore, applying Fourier transforms to (5.1) and interchanging the order of integration yields

$$\begin{aligned} \widehat{f}_m(\omega) &= \int_{\mathbf{R}} \int_{\mathbf{R} \setminus \{0\}} D(\tau, s) \int_{\mathbf{R}} |s|^{-1/2} h_m \left(\frac{t - \tau}{s} \right) e^{-i\omega t} dt \frac{ds d\tau}{s^2} \\ &= \int_{\mathbf{R} \setminus \{0\}} \widehat{D(\cdot, s)}(\omega) \widehat{h}_m(s\omega) |s|^{-3/2} ds. \end{aligned}$$

Hence, by employing the substitution $\sigma = s\omega$, we obtain

$$\begin{aligned} \widehat{f}_m(\omega) &= \int_{\mathbf{R} \setminus \{0\}} \widehat{D(\cdot, \frac{\sigma}{\omega})}(\omega) \widehat{h}_m(\sigma) \left| \frac{\sigma}{\omega} \right|^{-3/2} |\omega|^{-1} d\sigma \\ &= \langle \widetilde{D}(\omega, \cdot), \widehat{h}_m(\cdot) \rangle, \end{aligned} \quad (5.5)$$

where $\widetilde{D}(\omega, \sigma)$ is defined by

$$\widetilde{D}(\omega, \sigma) := \widehat{D\left(\cdot, \frac{\sigma}{\omega}\right)}(\omega) |\omega|^{1/2} |\sigma|^{-3/2}. \quad (5.6)$$

From (5.5), we observe that the quantities $\hat{f}_m(\omega)$ can be interpreted as the coefficients of $\widetilde{D}(\omega, \cdot)$ with respect to the set $\{\hat{h}_m\}_{m \in \mathbf{Z}}$. However, from Lemma 2.1 we know that this set also constitutes a frame with reciprocal frame $(\hat{h})^m = \frac{1}{(2\pi)} \widehat{h^m}$. Therefore, by using the identity

$$f = \frac{1}{(2\pi)} \sum_{m \in \mathbf{Z}} \langle f, \hat{h}_m \rangle \widehat{h^m}, \quad (5.7)$$

we may reconstruct $\widetilde{D}(\omega, \sigma)$ as

$$\widetilde{D}(\omega, \sigma) = \frac{1}{(2\pi)} \sum_{m \in \mathbf{Z}} \hat{f}_m(\omega) \widehat{h^m}(\sigma). \quad (5.8)$$

From (5.8), we can now also reconstruct the density $D(\tau, s)$. By using the definition (5.6) we obtain

$$\widehat{D\left(\cdot, \frac{\sigma}{\omega}\right)}(\omega) = \frac{1}{(2\pi)} \sum_{m \in \mathbf{Z}} \hat{f}_m(\omega) \widehat{h^m}(\sigma) |\sigma|^{3/2} |\omega|^{-1/2}$$

which yields

$$\widehat{D(\cdot, s)}(\omega) = \frac{1}{(2\pi)} \sum_{m \in \mathbf{Z}} \hat{f}_m(\omega) |\omega| \widehat{h^m\left(\frac{\cdot}{s}\right)}(\omega) |s|^{1/2}. \quad (5.9)$$

Now the result follows by applying the one-dimensional inverse Fourier transform to both sides of (5.9)

$$\begin{aligned} D(\tau, s) &= \frac{1}{(2\pi)} \int_{\mathbf{R}} \widehat{D(\cdot, s)}(\omega) e^{i\tau\omega} d\omega \\ &= \frac{1}{(2\pi)^2} \sum_{m \in \mathbf{Z}} \int_{\mathbf{R}} \hat{f}_m(\omega) |\omega| \widehat{h^m\left(\frac{\cdot}{s}\right)}(\omega) |s|^{1/2} e^{i\tau\omega} d\omega \\ &= \frac{1}{(2\pi)^2} \sum_{m \in \mathbf{Z}} \int_{-\infty}^0 -\frac{1}{i} \widehat{f'_m}(\omega) \widehat{h^m\left(\frac{\cdot}{s}\right)}(\omega) |s|^{1/2} e^{i\tau\omega} d\omega \\ &\quad + \frac{1}{(2\pi)^2} \sum_{m \in \mathbf{Z}} \int_0^{\infty} \frac{1}{i} \widehat{f'_m}(\omega) \widehat{h^m\left(\frac{\cdot}{s}\right)}(\omega) |s|^{1/2} e^{i\tau\omega} d\omega. \end{aligned}$$

□

From the mathematical point of view, Theorem 5.1 is clearly satisfactory. However, the applicability of this method to real-life problems is diminished by the fact that the underlying frame usually contains *infinitely* many elements. Clearly, in practice, only a finite number of frame elements can be transmitted. Hence we are faced with the problem of choosing appropriate collections. Furthermore, it is clearly desirable to have some information concerning the resulting approximation properties for different choices of frames.

5.2 Error Bounds in the Wideband Regime

The derivation of the error bounds rests on a Jackson type estimate for the frame $\{\widehat{h^m}\}_{m \in \mathbf{Z}}$. Let us assume that this set of functions allows an ordering by index sets $I_J \subset \mathbf{Z}$, s.t. a Jackson type estimate of the form

$$\|g - \frac{1}{(2\pi)} \sum_{m \in I_J} \langle g, \hat{h}_m \rangle \widehat{h^m}\|_{L_2(\mathbf{R})}^2 \lesssim 2^{-2J\alpha} |g|_{H^\alpha(\mathbf{R})}^2 \quad (5.10)$$

holds. Here H^α again denotes the Sobolev space of order α .

Such estimates are known for a variety of functions, e.g. trigonometric polynomials and hierarchical finite elements. In the context of wavelet analysis, this requirement is met by orthogonal or biorthogonal wavelets, compare with (2.19). If (5.10) is valid, the following result in the weighted L_2 -space $L_2(\mathbf{R}^2, d\tau \frac{ds}{|s|^3})$ holds.

Theorem 5.2 *Suppose that for some fixed α a Jackson-type estimate of the form (5.10) holds and that the condition*

$$G(\alpha, \omega) := |\widetilde{D}(\omega, \cdot)|_{H^\alpha(\mathbf{R})}^2 < \infty \quad (5.11)$$

is satisfied. Then, the following error estimate is valid:

$$\int_{\mathbf{R}} \int_{\mathbf{R}} \left| D(\tau, s) - \frac{1}{(2\pi)^2} \sum_{m \in I_J} \int_{\mathbf{R}} \hat{f}_m(\omega) \hat{h}_m(s\omega) |\omega||s|^{3/2} e^{i\tau\omega} d\omega \right|^2 d\tau \frac{ds}{|s|^3} \lesssim 2^{-2J\alpha} \int_{\mathbf{R}} |\omega| G(\alpha, \omega) d\omega. \quad (5.12)$$

If α is an integer, the function $G(\alpha, \omega)$ can be estimated in terms of the density D as follows:

$$G(\alpha, \omega) \lesssim \sum_{\beta \leq \alpha} |\omega|^{1+2\beta-2\alpha} \int_{\mathbf{R}} \left| \left(\frac{\partial}{\partial \sigma} \right)^{\alpha-\beta} \widehat{D}\left(\cdot, \frac{\sigma}{\omega}\right)(\omega) \sigma^{3/2-\beta} \right|^2 d\sigma. \quad (5.13)$$

Proof: In our setting, the Jackson-type estimate (5.10) applied to $g = \widetilde{D}(\omega, \cdot)$ reads as follows:

$$\|\widetilde{D}(\omega, \cdot) - \frac{1}{(2\pi)} \sum_{m \in I_J} \hat{f}_m(\omega) \hat{h}_m(\cdot)\|_{L_2(\mathbf{R})}^2 \lesssim 2^{-2J\alpha} |\widetilde{D}(\omega, \cdot)|_{H^\alpha(\mathbf{R})}^2, \quad (5.14)$$

Hence, by using (5.6) and substituting $\sigma = s\omega$ we obtain

$$\begin{aligned} 2^{-2J\alpha} G(\alpha, \omega) &\gtrsim \|\widehat{D}\left(\cdot, \frac{\sigma}{\omega}\right)(\omega) |\omega|^{1/2} |\sigma|^{-3/2} - \frac{1}{(2\pi)} \sum_{m \in I_J} \hat{f}_m(\omega) \hat{h}_m(\sigma)\|_{L_2(d\sigma)}^2 \quad (5.15) \\ &= \int_{\mathbf{R}} \left| \widehat{D}(\cdot, s)(\omega) - \frac{1}{(2\pi)} \sum_{m \in I_J} \hat{f}_m(\omega) \hat{h}_m(s\omega) |\omega||s|^{3/2} \right|^2 |\omega| |\omega|^{-2} \frac{ds}{|s|^3}. \end{aligned}$$

Therefore multiplying both sides of (5.15) by $|\omega|$, integrating with respect to ω and applying Plancherel's Theorem for another time yields

$$\begin{aligned} 2^{-2J\alpha} \int_{\mathbf{R}} |\omega| G(\alpha, \omega) d\omega &\gtrsim \int_{\mathbf{R}} \int_{\mathbf{R}} \left| \widehat{D(\cdot, s)}(\omega) - \frac{1}{(2\pi)} \sum_{m \in I_J} \hat{f}_m(\omega) \hat{h}_m(s\omega) |\omega| |s|^{3/2} \right|^2 d\omega \frac{ds}{|s|^3} \\ &= 2\pi \int_{\mathbf{R}} \int_{\mathbf{R}} \left| D(\tau, s) - \frac{1}{(2\pi)^2} \sum_{m \in I_J} \int_{\mathbf{R}} \hat{f}_m(\omega) \hat{h}_m(s\omega) |\omega| |s|^{3/2} e^{i\tau\omega} d\omega \right|^2 d\tau \frac{ds}{|s|^3}. \end{aligned} \quad (5.16)$$

For the proof of (5.13), we refer to [10]. □

Now let us consider the special case that the frames $\{h_m\}_{m \in \mathbf{Z}}$ and $\{h^m\}_{m \in \mathbf{Z}}$ consist of the inverse Fourier transforms of the elements of a biorthogonal wavelet basis, i.e.,

$$h_m = h_{m(j,k)} = \mathcal{F}^{-1} \psi_{j,k}, \quad h^m = h^{m(j,k)} = (2\pi) \mathcal{F}^{-1} \tilde{\psi}_{j,k}, \quad (5.17)$$

where the functions $\psi_{j,k}$ and $\tilde{\psi}_{j,k}$ satisfy

$$\langle \psi_{j,k}, \tilde{\psi}_{j',k'} \rangle = \delta_{j,j'} \delta_{k,k'}. \quad (5.18)$$

We may e.g. use the compactly supported wavelet basis constructed by Daubechies [14] or the biorthogonal wavelet basis developed by Cohen, Daubechies, and Feauveau [8]. Then we do not employ all functions in the resulting frame, but only those up to a given refinement level J . The resulting error estimate reads as follows.

Corollary 5.1 *Let $N - 1$ denote the degree of polynomial exactness of the multiresolution analysis $\{\tilde{V}_j\}_{j \in \mathbf{Z}}$ associated with the dual wavelet $\tilde{\psi}$. Suppose that for some fixed $\alpha < N$ the condition (5.11) holds. Then, the following error estimate is valid:*

$$\int_{\mathbf{R}} \int_{\mathbf{R}} \left| D(\tau, s) - \frac{1}{(2\pi)^2} \sum_{j \leq J} \int_{\mathbf{R}} \hat{f}_m(\omega) \hat{h}_m(s\omega) |\omega| |s|^{3/2} e^{i\tau\omega} d\omega \right|^2 d\tau \frac{ds}{|s|^3} \lesssim 2^{-2J\alpha} \int_{\mathbf{R}} |\omega| G(\alpha, \omega) d\omega. \quad (5.19)$$

Proof: Classical wavelet analysis provides us with the Jackson-type estimate

$$\|g - \sum_{k \in \mathbf{Z}, j \leq J} \langle g, \psi_{j,k} \rangle \tilde{\psi}_{j,k}\|_{L_2(\mathbf{R})}^2 \lesssim 2^{-2\alpha J} |g|_{H^\alpha(\mathbf{R})}^2, \quad (5.20)$$

see, e.g., [15] and Section 2 for details. Now the result follows from Theorem 5.1. □

Remark 5.1 *The polynomial exactness is closely related with the regularity of the wavelet basis, see [14] for details.*

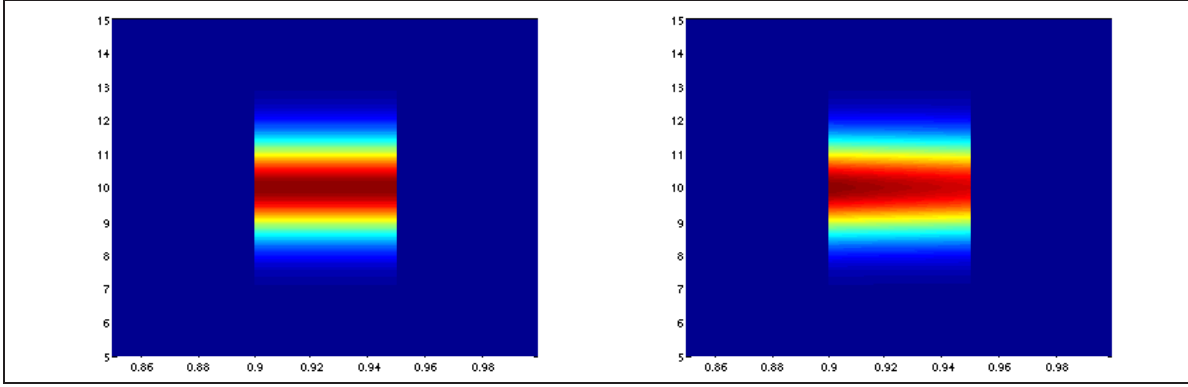


Figure 2: Representation of $\widehat{D}(\cdot, s)(\omega)$ and $\widehat{D}(\cdot, s)(\omega)|s|^{-3/2}$ on the discrete grid $[5.00, 15.00] \times [0.85, 1.00]$.

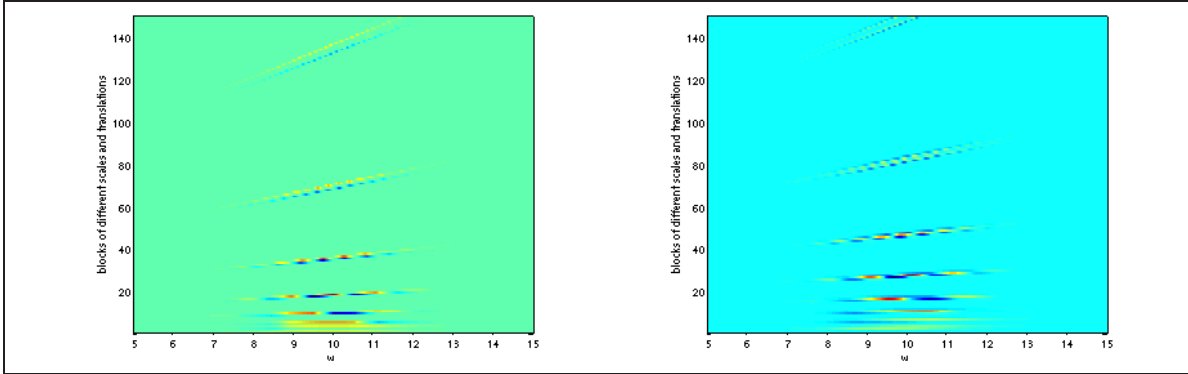


Figure 3: The simulated echos $\{\hat{f}_m\}_{m \in \mathbf{Z}}$ for the Haar frame (left-hand side) and for the Daubechies-5-frame (right-hand side). The higher scales are not displayed.

5.3 Numerical Experiments in the Wideband Regime

In this section, we want to demonstrate the applicability of our reconstruction formulas and the error estimates presented above. The application of our theory to real-life data is still in its elaboration. Nevertheless, to test the algorithm, we proceed as follows. We fix in advance an (artificial) density D in range Doppler coordinates and a suitable frame $\{h_m\}_{m \in \mathbf{Z}}$, compute the corresponding echos and apply the reconstruction procedure to these echos. Since in this case the density is known, this approach allows some meaningful comparisons.

Primary, we fix a density D which fits into the setting and a frame $\{h_m\}_{m \in \mathbf{Z}}$. As an manageable example we choose D as

$$D(\tau, s) := e^{i\tau\omega_0} e^{-\tau^2/2} 1_{[-s_1, s_2]}(s),$$

where $1_{[-s_1, s_2]}$ represents the characteristic function of the closed interval $[-s_1, s_2]$ and ω_0 describes a shift in Fourier domain. In the sequel, we choose $s_1 = 0.90$ and $s_2 = 0.95$. The assumption of Theorem 5.1 on D are satisfied. The outgoing signal has to be a frame. However,

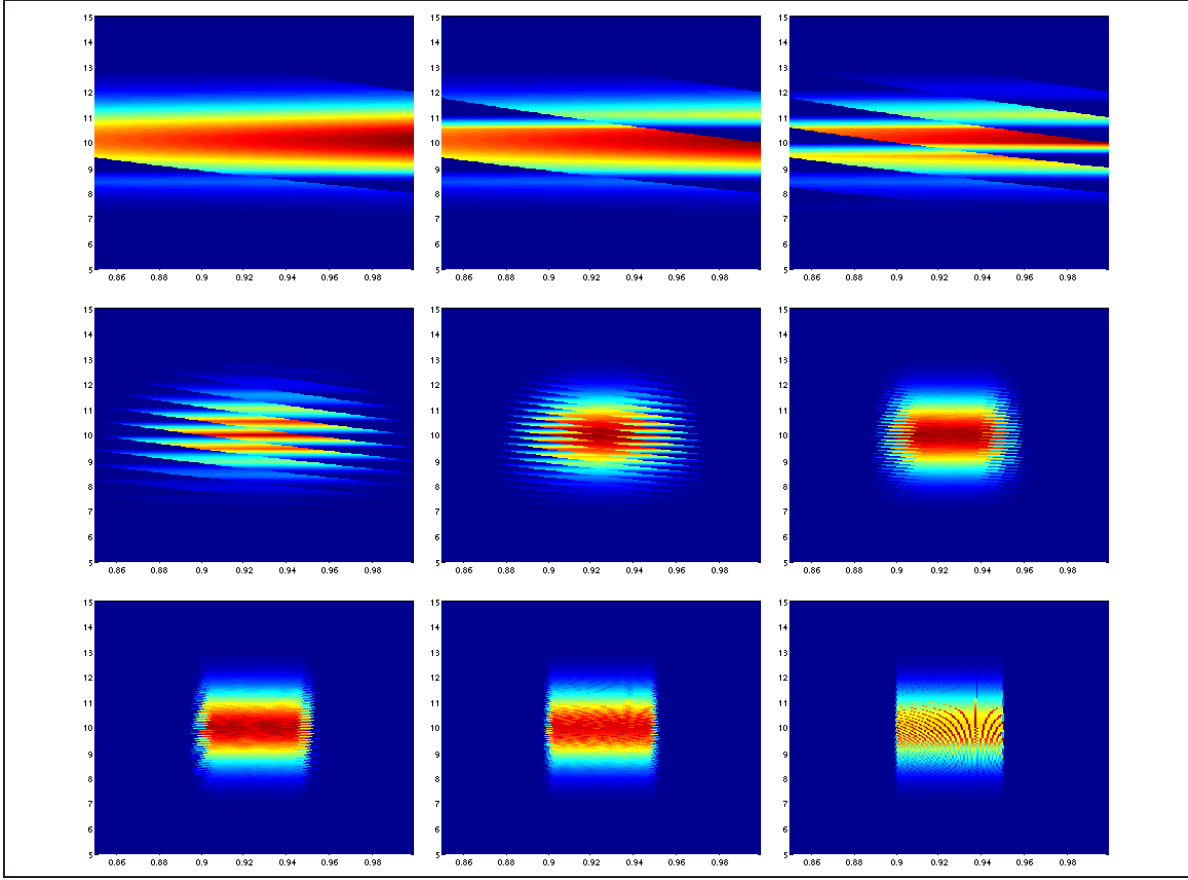


Figure 4: Partial reconstructions based on simulated echos with respect to the Haar frame. The shown images correspond to the reconstructed densities for $J = -3, -2, -1, 0, 1, 2, 3, 4$ and 6 (from top left to bottom right).

since we also want to check the error estimate in Theorem 5.1, a straightforward choice for the frame is

$$h_m(t) = h_{m(j,k)}(t) := \mathcal{F}^{-1}\psi_{j,k}(t),$$

where $\mathcal{F}^{-1}\psi_{j,k}$ is the inverse Fourier transform of some dilated and translated wavelet, see formula (5.17). In our simulations we used the Haar basis, the Daubechies wavelets of order two, compare [14], and biorthogonal wavelets as constructed in [8], respectively.

Based on the underlying density D we may generate families of echos $\{f_m\}_{m \in \mathbf{Z}}$ which represent the backscattered families of the transmitted frame $\{h_m\}_{m \in \mathbf{Z}}$. Numerically we have to truncate the evaluation of the echos at some index (j, k) . The numerical implementations start at resolution level $j_{\min} = -3$ and end at $j_{\max} = 6$. At the first approximation level $j_{\min} = -3$ we use the echos produced by translates of the corresponding generator function φ . The resulting echos are visualized in Figure 3.

Now we are ready to apply the reconstruction formula stated in Theorem 5.1. To examine the

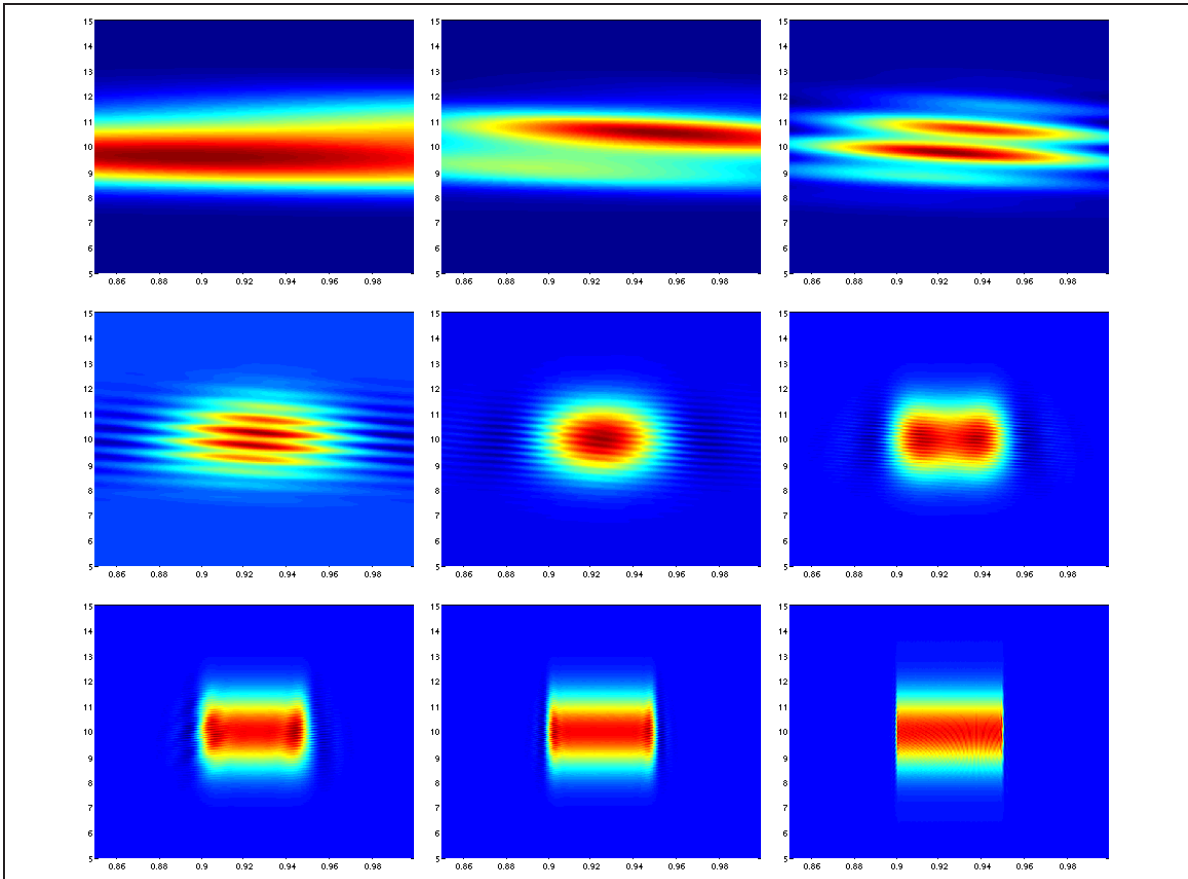


Figure 5: Partial reconstructions based on simulated echos with respect to the Bior2.8 frame. The shown images correspond to the reconstructed densities for $J = -3, -2, -1, 0, 1, 2, 3, 4$ and 6 (from top left to bottom right).

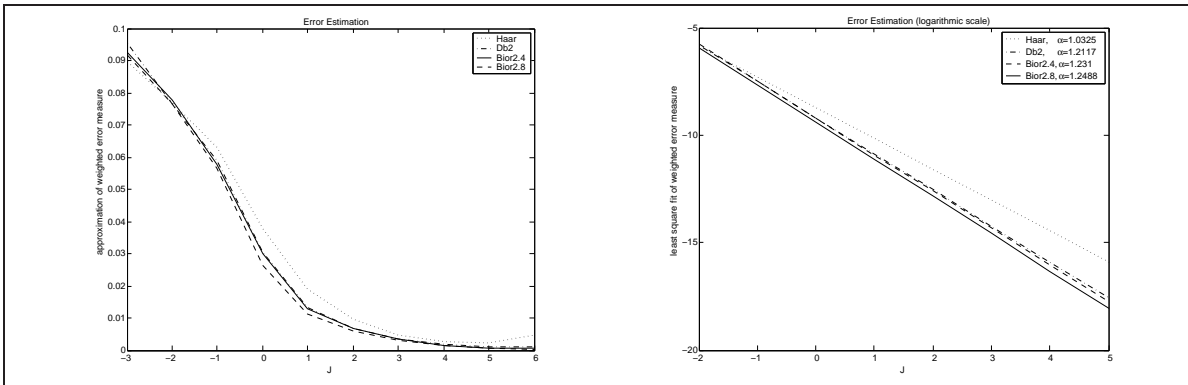


Figure 6: The weighted L_2 -error. The left-hand side shows the numerically evaluated error and the right-hand side the linear least square fit in the logarithmic scale.

quality of the reconstruction we compute the left hand side of the error estimate of Theorem 5.2. Theorem 5.2 predicts an exponential decay of the error rate with constants depending on the frame regularity. And indeed, we observe that the weighted L_2 -error decreases in the predicted way as the frame regularity increases. To show successively these results, we start by presenting a scale-wise reconstruction, see Figures 4 and 5. It turns out that the algorithm converges for all simulated cases. Following Theorem 5.2 we study the error depending on the scale J and on the frame regularity α , respectively. From Figure 6, left image, we observe that the error indeed decreases exponentially. From the logarithmic plot, right image, we can estimate the parameter α as the slope of the linear least square fit, compare with Figure 6. We deduce the validity of the proposed wavelet based reconstruction algorithm and the given error estimate. Therefore the first numerical results confirm our theory.

5.4 Basic Reconstruction Formulas in the Narrowband Regime

Similar to the wideband approach, the goal in this section is clearly to reconstruct the narrowband density function $D_{NB}(\phi, \tau)$ from the received echoes. It turns out that a suitable reconstruction formula can indeed be derived, provided that the families of outgoing signals form frames in the spaces $L_{2,P}(\mathbf{R})$ and $L_{2,R}(\mathbf{R})$, respectively.

Theorem 5.3 *Let $\{h_m\}_{m \in \mathbf{Z}}$, $\{g_m\}_{m \in \mathbf{Z}}$ be sets of outgoing signals in $L_{2,P}(\mathbf{R})$ and $L_{2,R}(\mathbf{R})$, respectively. Let us furthermore assume that $\{h_m\}_{m \in \mathbf{Z}}$, $\{g_m\}_{m \in \mathbf{Z}}$ form frames in these spaces, and let $\{h^m\}_{m \in \mathbf{Z}}$ and $\{g^m\}_{m \in \mathbf{Z}}$ denote the corresponding dual frames. The echoes of $\{h_m\}_{m \in \mathbf{Z}}$ are denoted by $f_{P,m}$, the echoes of $\{g_m\}_{m \in \mathbf{Z}}$ are denoted by $f_{R,m}$. Let us assume that the reflectivity density $D_{NB}(\phi, \tau)$ satisfies the following conditions*

$$h_m(t - \tau)D_{NB}(\phi, \tau) \in L_1(d\phi d\tau), \quad \widehat{D_{NB}(\cdot, \tau)}(\omega) \in L_1(d\omega). \quad (5.21)$$

Then $D_{NB}(\phi, \tau)$ can be reconstructed as follows

$$\begin{aligned} D_{NB}(\phi, \tau) &= \frac{1}{2\pi} \sum_{m \in \mathbf{Z}} \int_{\mathbf{R}} f_{P,m}(t) h^m(t - \tau) e^{i\phi t} dt \\ &\quad + \frac{1}{2\pi} \sum_{m \in \mathbf{Z}} \int_{\mathbf{R}} f_{R,m}(-t) g^m(-t - \tau) e^{i\phi t} dt. \end{aligned} \quad (5.22)$$

Proof: We proceed by following the lines of the proof of Theorem 2.2 in [11]. Using (4.13) yields

$$\begin{aligned} f_{P,m}(t) &= \int_{\mathbf{R}} \int_{\mathbf{R}} e^{-i\phi t} h_m(t - \tau) D_{NB}(\phi, \tau) d\phi d\tau \\ &= \int_{\mathbf{R}} h_m(t - \tau) \left(\int_{\mathbf{R}} e^{-i\phi t} D_{NB}(\phi, \tau) d\phi \right) d\tau \end{aligned}$$

$$\begin{aligned}
&= \int_{\mathbf{R}} h_m(t - \tau) \widehat{D_{NB}(\cdot, \tau)}(t) d\tau \\
&= \int_{\mathbf{R}} h_m(\tau) \widehat{D_{NB}(\cdot, t - \tau)}(t) d\tau \\
&= \langle h_m(\cdot), (\widetilde{D_{NB}}(t, \cdot))_P \rangle_{L_2(\mathbf{R})},
\end{aligned}$$

where

$$\widetilde{D_{NB}}(t, \tau) := \widehat{D_{NB}(\cdot, t - \tau)}(t). \quad (5.23)$$

Consequently, by using the reciprocal frame $\{h^m\}_{m \in \mathbf{Z}}$ and exploiting the fundamental reconstruction formula (2.57), we obtain

$$\begin{aligned}
(\widetilde{D_{NB}}(t, \tau))_P &= \sum_{m \in \mathbf{Z}} \langle (\widetilde{D_{NB}}(t, \cdot))_P, h_m(\cdot) \rangle_{L_2(\mathbf{R})} h^m(\tau) \\
&= \sum_{m \in \mathbf{Z}} f_{P,m}(t) h^m(\tau),
\end{aligned}$$

and therefore

$$(\widehat{D_{NB}(\cdot, \tau)}(t))_P = \sum_{m \in \mathbf{Z}} f_{P,m}(t) h^m(t - \tau). \quad (5.24)$$

A similar calculation yields

$$\begin{aligned}
(\overline{D_{NB}}(t, \tau))_R &= \sum_{m \in \mathbf{Z}} \langle (\overline{D_{NB}}(t, \cdot))_R, g_m(\cdot) \rangle_{L_2(\mathbf{R})} g^m(\tau) \\
&= \sum_{m \in \mathbf{Z}} f_{R,m}(t) g^m(\tau)
\end{aligned}$$

where

$$\overline{D_{NB}}(t, \tau) := \widehat{D_{NB}(\cdot, t - \tau)}(-t). \quad (5.25)$$

Consequently, we obtain

$$(\widehat{D_{NB}(\cdot, \tau)}(-t))_R = \sum_{m \in \mathbf{Z}} f_{R,m}(t) g^m(t - \tau) \quad (5.26)$$

so that

$$(\widehat{D_{NB}(\cdot, \tau)}(t))_R = \sum_{m \in \mathbf{Z}} f_{R,m}(-t) g^m(-t - \tau) \quad (5.27)$$

and

$$\begin{aligned}
\widehat{D_{NB}(\cdot, \tau)}(t) &= (\widehat{D_{NB}(\cdot, \tau)}(t))_R + \widehat{D_{NB}(\cdot, \tau)}(t)_P \\
&= \sum_{m \in \mathbf{Z}} f_{P,m}(t) h^m(t - \tau) + \sum_{m \in \mathbf{Z}} f_{R,m}(-t) g^m(-t - \tau).
\end{aligned}$$

Now the result follows by applying the inverse Fourier transform

$$\begin{aligned}
D_{NB}(\phi, \tau) &= \frac{1}{2\pi} \int_{\mathbf{R}} \widehat{D_{NB}(\cdot, \tau)}(t) e^{i\phi t} dt \\
&= \frac{1}{2\pi} \sum_{m \in \mathbf{Z}} \int_{\mathbf{R}} f_{P,m}(t) h_m(t - \tau) e^{i\phi t} dt \\
&\quad + \frac{1}{2\pi} \sum_{m \in \mathbf{Z}} \int_{\mathbf{R}} f_{R,m}(-t) g^m(-t - \tau) e^{i\phi t} dt.
\end{aligned}$$

□

6 Analysis of Discrete Radar Wind Profiler Data

This section is concerned with the determination of the three dimensional atmospheric wind vector field on the basis of real radar wind profiler (RWP) measurements. Due to the nature of those instruments we are not able to apply the established reconstruction formulas from the wideband and narrowband regime, respectively. However, there is another aspect where wavelets play a important role. To discuss the difficulties in practical radar applications and to demonstrate the benefit of wavelets we proceed as follows: First, we briefly describe some characteristics of radar wind profilers, secondly, we explain the specific problems in profiler radar signal processing, and thirdly, we present a wavelet based method to improve the preprocessing of those radar data. The wavelet preprocessing uses a multiscale approach as explained in Section 2.1 and the statistical techniques outlined in Section 3.

6.1 Radar Wind Profilers

The RWP is a special application of Doppler radar technology and is now increasingly used to routinely probe the vertical profile of the mean horizontal wind in the earth's atmosphere. The data are mainly used for weather forecasting and environmental monitoring. Most currently used RWP's employ the so-called 'Doppler beam swinging' method (DBS) for wind determination. The range of applications for these systems is certainly wider then it is mentioned here, but this is beyond the scope of this paper. More details about the use of coherent radar technology and in particular wind profilers in meteorology can be found in standard textbooks [17, 22] and in several review papers, e.g. [46].

For RWP's, the Doppler shift and therefore the radial velocity of the scatterers is determined using different beam directions. For wind determination, there are of course at least three linear independent beam directions and some assumptions concerning the wind field required to transform the measured 'line-of-sight' radial velocities into the wind vector. This principle will be briefly shown for a five beam system as depicted in Figure 7. We assume that the wind field \vec{v} with components

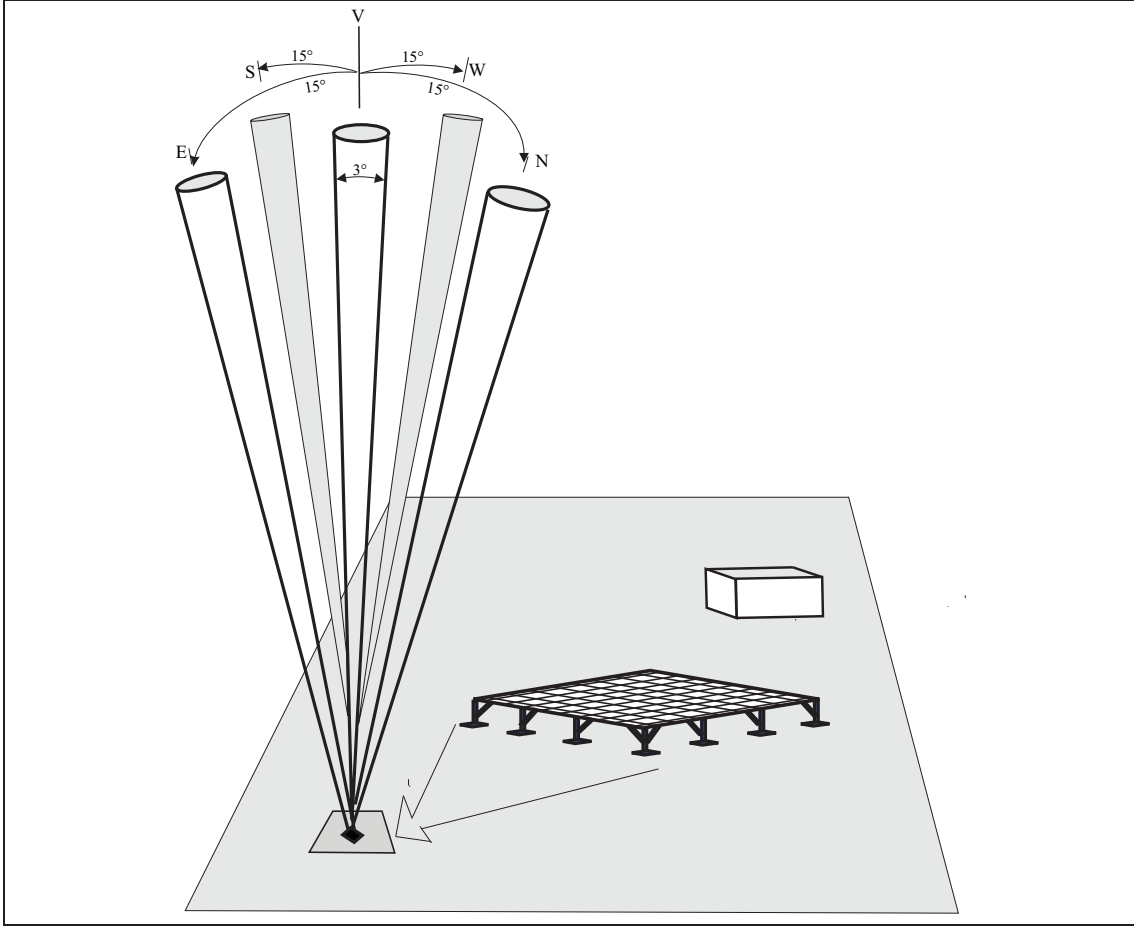


Figure 7: Beam configuration of a typical DBS radar wind profiler

(u, v, w) in a Cartesian coordinate system in the vicinity of the radar can be written as a linear Taylor series expansion in the horizontal coordinates

$$\vec{v}(x, y, z) \doteq \vec{v}(x_0, y_0, z) + \nabla_h \vec{v}(x, y, z)|_{x_0, y_0} \cdot \Delta \vec{r}, \quad (6.1)$$

where $(x_0, y_0, 0)$ denotes the location of the transmitter/receiver. If the radial velocity measured in the ‘line-of-sight’ of a radar beam described by unit directional vector \vec{n} is written as

$$v_r = \vec{v} \cdot \vec{n}, \quad (6.2)$$

then, we get for the differences of the radial winds of the four oblique beams at height z

$$\begin{aligned} v_{rE}(z) - v_{rW}(z) &= 2u_0(z) \sin(\alpha) + 2 \frac{\partial w}{\partial x} z \cos(\alpha) \tan(\alpha) \\ v_{rN}(z) - v_{rS}(z) &= 2v_0(z) \sin(\alpha) + 2 \frac{\partial w}{\partial y} z \cos(\alpha) \tan(\alpha), \end{aligned}$$

where $u_0(z)$ denotes the horizontal West-East wind component at height z , $v_0(z)$ denotes the horizontal North-South wind component at height z , α denotes the zenith distance of the oblique beams and the subscripts denote East, West, North and South, respectively. It is immediately clear that one additional assumption is required to determine the (horizontal) wind components (u_0, v_0) , namely:

$$\frac{\partial w}{\partial x} = \frac{\partial w}{\partial y} = 0.$$

In meteorological language, the horizontal shear of the vertical wind must vanish to retrieve the horizontal wind without errors. This condition is not always given, however, it is usually correct over a longer time interval. Therefore, DBS RWP's can only be used to determine the averaged wind.

Here and henceforth we will only be concerned with the determination of the radial velocity along one beam. This is the main focus of signal processing for RWP's. Strictly speaking, signal processing includes all operations that are performed on the received voltage signal at the antenna output, including the analog operations employed before A/D conversion, that is signal amplification, frequency down-conversion and filtering. However, we will only deal with digital signal processing (after A/D conversion), cp. Figure 8, which has the purpose to extract the desired atmospheric information from the received voltage signal.

RWP's transmit a series of short electromagnetic pulses (each one separated by a time ΔT) in a fixed beam direction and sample the backscattered signal received by the antenna to determine the Doppler shift. For a single pulse, the sampling in time allows the determination of the radial distance of the measurement using the well-known propagation speed of the radar wave (ranging). The maximum distance for unambiguously determining the measurement distance is clearly determined by the pulse separation ΔT , namely $d_{max} = c\Delta T/2$, it is called the maximum unambiguous range. It has to be set sufficiently high to prevent range aliasing problems, that is arrival of backscattering signals from the first pulse after the transmission of the next pulse.

The bandwidth B of a transmitted pulse of duration δt is typically much larger ($B = C \cdot 1/\delta t \approx 100 \dots 1000$ kHz, for some constant $C > 0$) than the Doppler shift for atmospheric scatterers ($f_d < 500$ Hz), which prevents a precise measurement of the Doppler shift from a single pulse. For that reason a time series is generated for each and every range gate by sampling a whole series of transmit pulses. The Doppler frequency is then determined from the slowly changing phase of the received signals, see [4], using a quadrature demodulator and is further used to determine the velocity component of 'the atmosphere' projected onto the beam direction ($f_D = 2v_r/\lambda$). The sampling is usually done in the process of A/D conversion of the received signal and the sampling rate for the discrete time series (4.25) at each range gate is of course determined by the pulse repetition period ΔT .

The main goals of radar signal processing as summarized in [31] are:

- to provide accurate, unbiased estimates of the characteristics of the desired atmospheric echoes;
- to estimate the confidence/accuracy of the measurement;

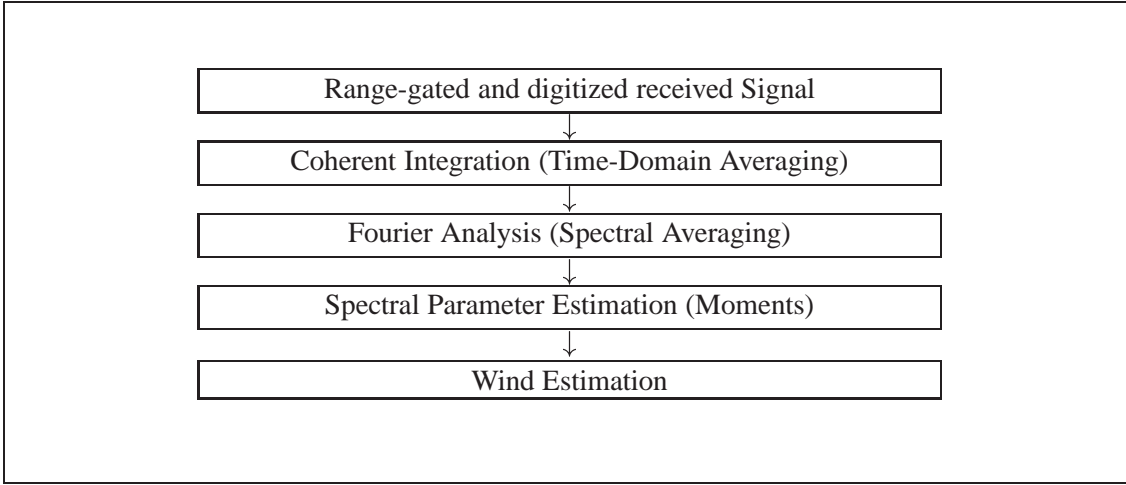


Figure 8: The Fig. shows the flow diagram of 'classical' digital signal processing.

- to mitigate effects of interfering signals;
- to reduce the data rate.

As outlined in Section 4.4, the complex envelope determined by a quadrature demodulation can be written as

$$\tilde{f}_h(t) = \tilde{I}(t) + i\tilde{Q}(t) ,$$

see formula (4.25) and see [34]. The signal \tilde{f}_h forms for atmospheric scattering a complex Gaussian random process in time [54], with sample points for each transmitted radar pulse. Such a process is fully described by 3 parameters, namely

- Signal power;
- Mean frequency (shift);
- Spectral width.

If $S(\omega)$ denotes the power spectrum associated with the random process signal then the fundamental parameters are the power P ,

$$P = \int S(\omega)d\omega ,$$

the mean Doppler shift Ω ,

$$\Omega = \frac{1}{P} \int \omega S(\omega)d\omega ,$$

and the velocity variance W^2 :

$$W^2 = \frac{1}{P} \int (\omega - \Omega)^2 S(\omega)d\omega .$$

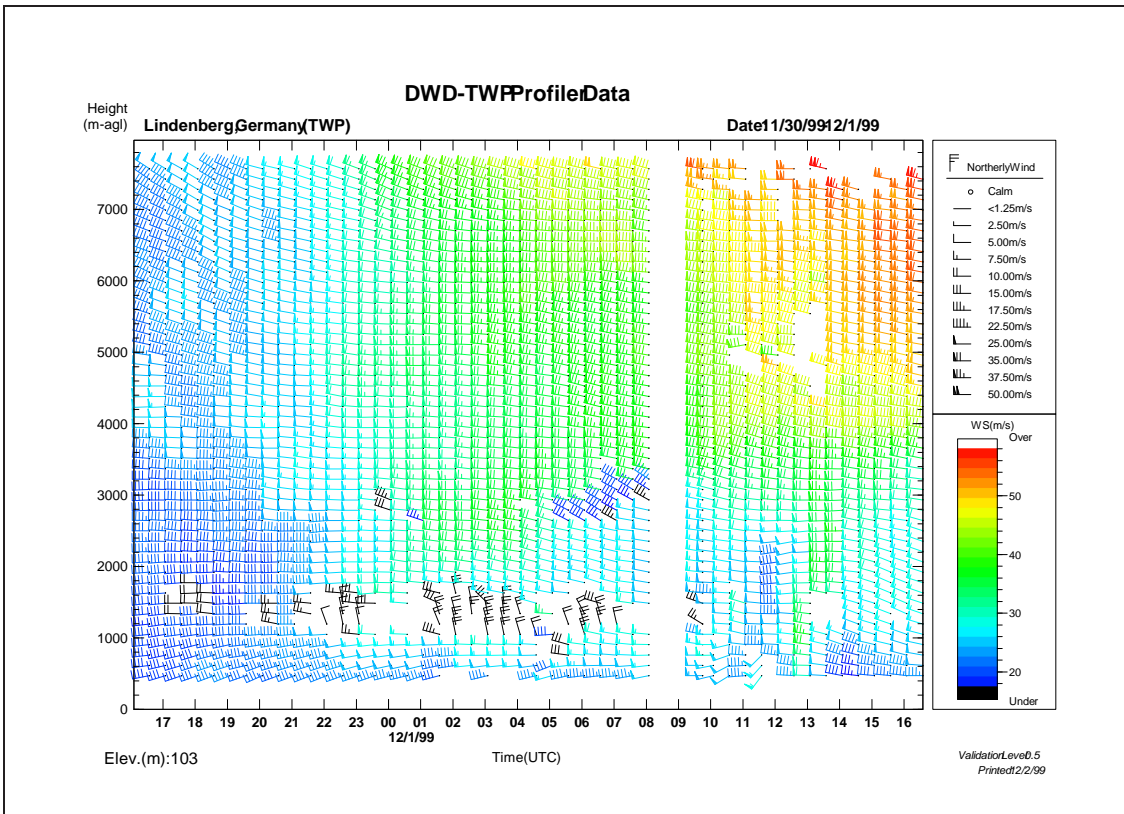


Figure 9: The Fig. shows the final result of the measurement with the 482 MHz RWP at Lindenberg (Germany) on the 30th November and 01st December 1999. The wind barbs are color coded according to the wind speed. Note the effects of the persistent ground clutter around 1.5 km and 3 km height. The gap in the data was caused by this detailed investigation as the radar was programmed to store time series data for about 30 minutes in the East beam only, thus no wind computations were possible for that period of time.

The goal of radar signal processing is consequently just the estimation of these 3 basic parameters and it therefore suffices to estimate the power spectral density (the so-called Doppler spectrum) of the given signal. The generally used procedure employs the fast Fourier transform and has the advantage of being non-parametric, i.e. no specific form of the spectrum is assumed. This is of advantage when the above mentioned assumptions are not fulfilled, however, the 3 base parameters are still uniquely defined, for details see [53].

Radar signal processing ends with the estimation of the moments of the Doppler spectrum and further data processing is then performed to finally determine the wind and other meteorological parameters using measurements from all radar beams, see Figure 9 and 10. To compute the Doppler frequency we thus use the discrete Fourier transform of f_h which is in detail given below.

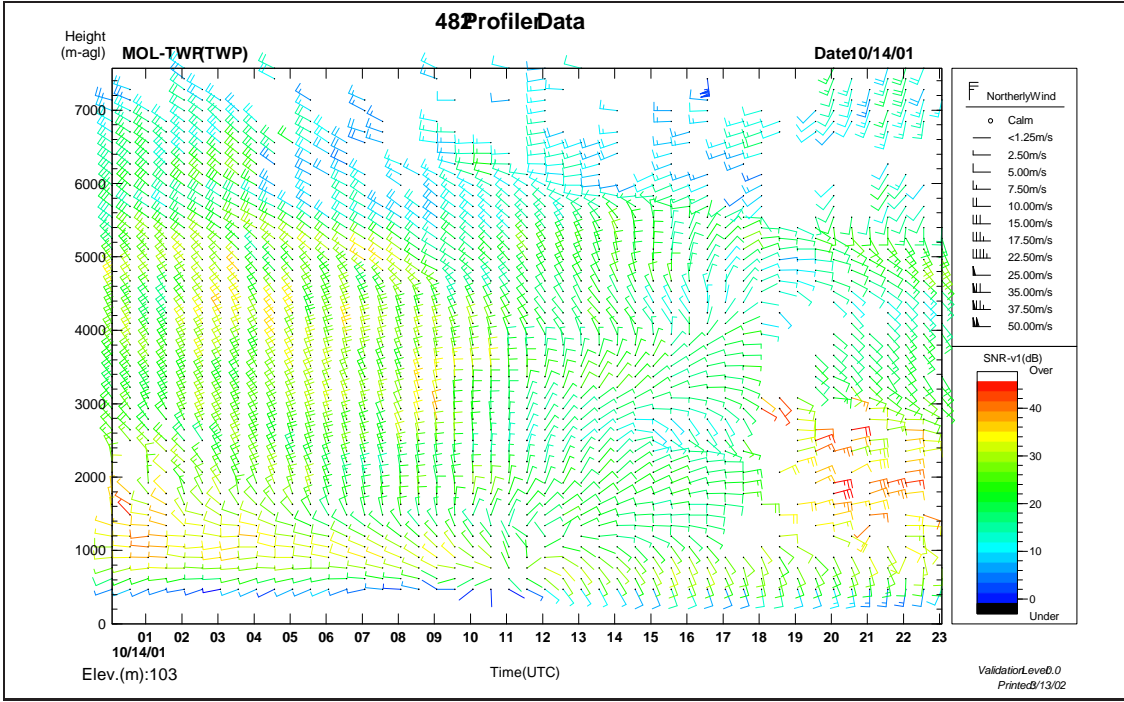


Figure 10: The Fig. shows the final result of the measurement with the 482 MHz RWP at Lindenberg (Germany) on the 14th October 2001. The wind barbs are color coded according to the wind speed. The distinct maxima in wind speed after sunset between 1 and 3 km height are caused by dense bird migration, that could not be eliminated by the applied processing, even when the statistical averaging method proposed in [38] was used.

6.2 Problems in RWP Signal Processing

The typically implemented radar signal processing flow in RWP's is visualized in Figure 8. Digital signal processing starts with the determination of the complex envelope of the received signal which yields the in- and quadrature phase components (4.25). The sampling rate is determined by the pulse repetition period T . To reduce the data rate for further processing, hardware adder circuits perform a so-called coherent integration, adding L (typically ten to hundred) complex samples together. Mathematically, this operation can be seen as a filtering, followed by an under-sampling at a rate of $L \cdot T$

$$\overline{f_h(n)} = \frac{1}{L} \sum_{k=nL}^{(n+1)L} \tilde{f}_h(k).$$

The coherently averaged samples \overline{f}_h are then used to estimate the Periodogram (the Doppler spectrum) using the discrete windowed Fourier transform, see [5]

$$P_h(k) = \frac{1}{N} \left| \sum_{n=0}^{N-1} g(n) \overline{f}_h(n) e^{-j \frac{2\pi k n}{N}} \right|^2.$$

A number L' (typically some ten) of individual Doppler spectra is then incoherently averaged to reduce the noise variance of the Periodogram, thus improving the detectability of the signal, see [50]

$$\overline{P_h(k)} = \frac{1}{L'} \sum_{n=h}^{h+L'} P_n(k) .$$

Finally, the noise level is estimated with the method proposed in [26] and the moments of the maximum signal in the spectrum is computed over the range where the signal is above the noise level. This effectively avoids any unwanted noise contribution to the estimated moments and is equivalent with subtracting the noise level before deriving the moments, compare with [37, 48].

The problem with this type of signal processing is the underlying assumption, that the signal consists of only two parts:

$$y = f_a + \varepsilon , \quad (6.3)$$

where f_a is produced by the (Gaussian) atmospheric scattering process and ε is some noise of different sources, mainly thermal electronic noise and cosmic noise. This is certainly not true. Especially at UHF, the desired atmospheric signal itself is often the result of two distinct scattering processes, namely scattering at inhomogeneities of the refractive index (Bragg scattering) and scattering at particles like droplets or ice crystals (Rayleigh scattering), see for instance [21, 23, 22, 42, 43] . So, even the desired atmospheric signal may have different characteristics. But, as the experience shows, the most serious problems are caused by the following contributions to the signal:

$$y = f_a + f_g + f_i + f_r + \varepsilon , \quad (6.4)$$

where f_g is ground clutter, i.e. echoes returned from the ground surrounding the site, which emerge from antenna side-lobes, f_i is intermittent clutter, i.e. echoes returned from unwanted targets like airplanes or birds from both, the antennas main lobe and the side-lobes, and f_r is radio frequency interference which can emerge from external radio-frequency transmissions within the passband of the receiver (matched filter) or it can be generated internally due to imperfections of the radar hardware. An additional complication lies in the observed fact, that both f_i and f_r are generally not Gaussian.

6.3 Improved RWP Signal Processing by Wavelet Techniques

Recently, much work has been and continues to be done to develop frequency domain processing algorithms. The purpose of all these methods is to select the ‘true’ atmospheric signal even in the presence of severe contamination and perform moment estimation only with them. Unfortunately, practical success has been limited, mostly because the generation of the Doppler spectrum was not optimal:

- The use of coherent integration ‘pre-filters’ the time series and my cause unnecessary aliasing of airplane echoes into the frequency band of interest, for instance.
- The non-Gaussian characteristics of transient signal components (airplanes, birds) may render the DFT-based technique for spectral estimation useless.

In the following, we will therefore concentrate on the applicability of nonlinear wavelet filtering to ‘clean’ the time series before employing the DFT. The main reasons for the particular effectiveness of wavelet analysis are the facts that contamination appears often instationary or transient and with a priori unknown scale structure, that one can use a great variety of wavelet filters, and at least that the fast wavelet transform has a computationally complexity that is lesser than or equal to the fast Fourier transform.

For our purpose, we assume that the Gaussian model describes both, the atmospheric scattering component and the ground clutter signal sufficiently well. The transient nature of intermittent clutter returns can be sufficiently well described by the simple model given by [2]. A more detailed, exemplary look into the raw data (coherently integrated I/Q-Time series) of Gate 11 and 17 and the resulting power spectra, see Figure 11, reveals obviously that advanced signal processing for RWP is necessary to increase the accuracy of wind vector reconstruction: The time series at Gate 11 shows the typical signature of a ground clutter signal component, which corresponds to the narrow spike centered around zero (Doppler shift) in the resulting power spectrum. Additionally, the time series at Gate 17 shows a strong transient component in the last quarter.

Nonlinear wavelet filtering starts by applying the multiscale setting as in Section 2. For our purpose we assume that the measured complex-valued signal \tilde{f}_h can be interpreted as the projection on a subspace V_{j_0} . The estimation of the projection is given by (3.2) with coefficients as in (3.3). In comparison with ‘classical’ nonlinear wavelet de-noising we *reverse* the roles of the noise part ξ and f in the regression model (3.1), i.e., we assume that the atmospheric component f_a belongs to ξ and we interpret the oscillating clutter components as the signal f . Hence, the goal is to detect the clutter instead of the atmospheric echo. Once we have detected the clutter component, we only have to eliminate it from the signal \tilde{f}_h .

Consequently, to adapt the nonlinear wavelet filtering step to our problem we have to redefine the selection procedure for the coefficients as follows

$$\eta_h(x, t) = x - \theta_h(x, t) . \quad (6.5)$$

Then, by (6.5) we perform the necessary filtering step by the truncated hard threshold wavelet estimator (3.8). The common hard thresholding used for de-noising and the new definition are displayed Figure 12. The threshold definition (6.5) can be easily expressed by

$$\eta_h(u, t) = \begin{cases} u, & |u| < t \\ 0, & |u| \geq t \end{cases} ,$$

where t is a adequate threshold. To appraise the estimator it is known that we measure the expected loss or the risk, see Section 3,

$$\sup_{f \in \mathcal{F}_p^\alpha(M, T)} E \|f_n^* - f\|_{p'}^{p'} .$$

However, in our application we are interested in the situation $1 \leq p \leq 2$ and $p' = 2$. By the assumption $\alpha > 1/p$ we obtain that

$$\epsilon = \frac{p}{2} (2\alpha + 1) - 1 > 1/2 .$$

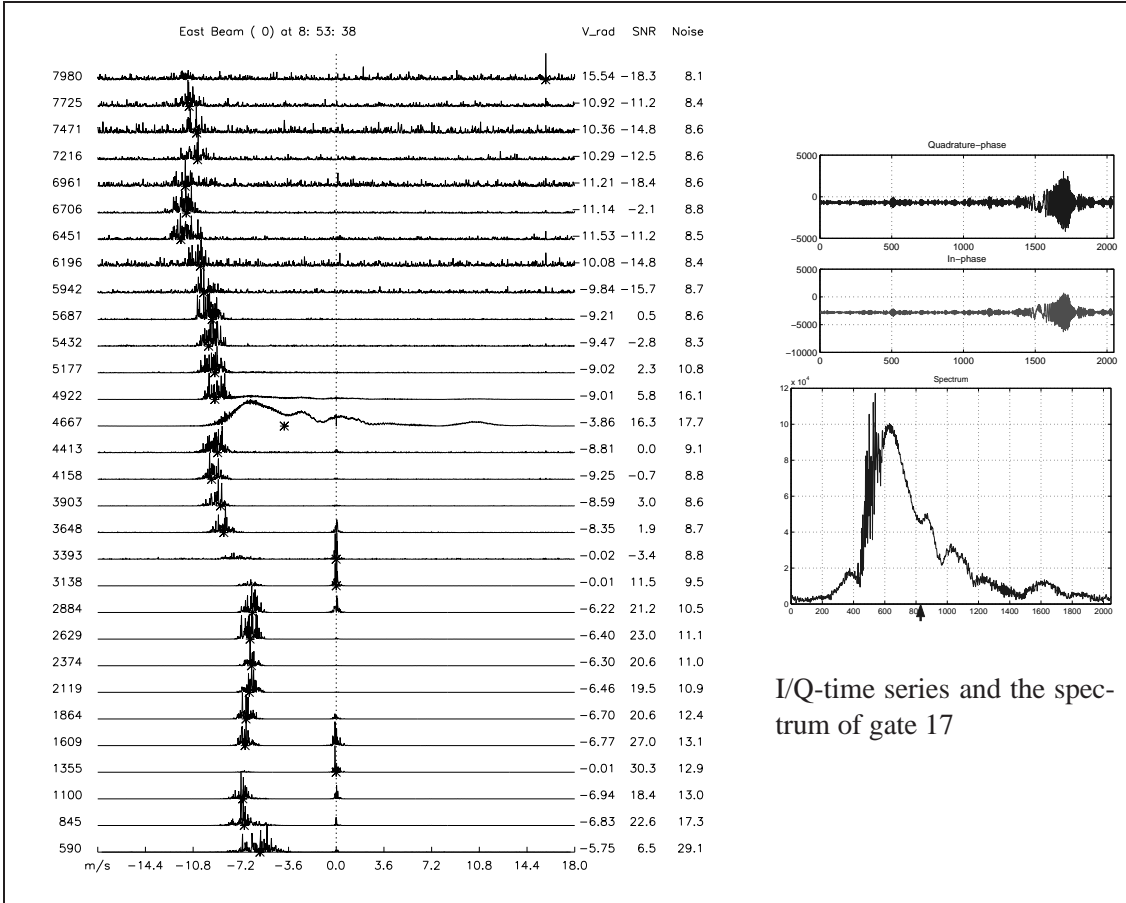


Figure 11: The left part shows the ‘stacked spectrum’ plot, i.e. the Doppler spectra for each range gate, for the radar dwell at 08:53:38 UTC on December 1st, 1999. The right figures give a detailed look into the raw data (I/Q-time series) and the Doppler spectrum for the gate 17 (whose data will be wavelet processed). The black arrows indicate the estimated first moment (i.e. the radial velocity).

Thus, for a positive constant C , we have the following asymptotic behavior for the risk function, see inequality (3.10),

$$\sup_{f \in \mathcal{F}_p^\alpha(M,T)} E \|f_n^* - f\|_2^2 \leq C (\log n)^{\frac{2-p}{2\alpha+1}} n^{\frac{-2\alpha}{2\alpha+1}}. \quad (6.6)$$

Remark 6.1 For the special case $p = 2$ we know that \mathcal{F}_2^α coincides with a ball in H^α , see [27] and (3.6).

For a numerical implementation one has to determine the scales j_1 and j_0 . In accordance to Theorem 3.1 and our specific setting we have $\delta = \alpha/(2\alpha + 1)$, i.e.,

$$2^{j_1(n)} \simeq \left(n (\log n)^{\frac{2-p}{p}} \right)^{\frac{1}{2\alpha+1}} \quad \text{and} \quad 2^{j_0(n)} \simeq n^{\frac{2p\alpha}{(2\alpha+1)(p(2\alpha+1)-2)}},$$

m	6	7	8	9	10	11	12	13	14	15	16	17	18	19	20
$j_1(2^m)$	3	4	4	4	5	5	6	6	6	7	7	7	8	8	8
$j_0(2^m)$	4	5	6	6	7	8	8	9	10	10	11	12	12	13	14

Table 1: A Table of suitable resolution levels j_1 and j_0 for a special choice of p and α , ($p = 1$, α close to 1).

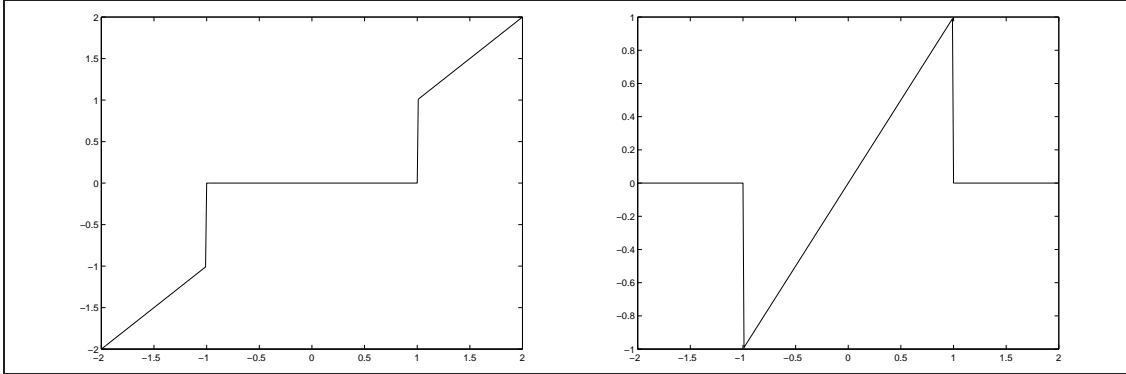


Figure 12: This Figure shows hard (left) and inverse hard thresholding (right) for $t = 1$.

see Table 1 for suitable resolution levels j_1 and j_0 . The choice of t can be implemented by applying the rule (3.11). Finally, the computation of the wavelet coefficients can be done by using the fast wavelet algorithm as described in Section 2.

6.4 Numerical Examples

In this section, we want to demonstrate the performance of our modified nonlinear wavelet filtering. This is done with both, simulated and real data. For a better understanding we particularize Figure 8 to see where we have inserted the wavelet filtering step. To clarify our procedure a more substantiated algorithm flow diagram is shown in Figure 13.

Additionally one may use histogram informations. The histogram displays the empirical distribution of the coefficients $\bar{\lambda}_k$ and $\bar{\gamma}_k^j$. In particular, if the signal was contaminated by an airplane echo the main part of observations is concentrated in a small neighborhood around zero. If there is no airplane echo the coefficients are exponentially distributed, see Figure 14.

To observe how this algorithm works we start by simulating one easy test sample. Using the statistical-stochastic approach of [56] to generate I/Q-time series, we first generate an atmospheric signal with Gaussian characteristic in the frequency domain. We choose the Doppler frequency of the atmospheric signal close to zero to force the separation problem. Now we add a noise variable and a ground clutter peak, which is generated by a narrow Gaussian. The order of the ground

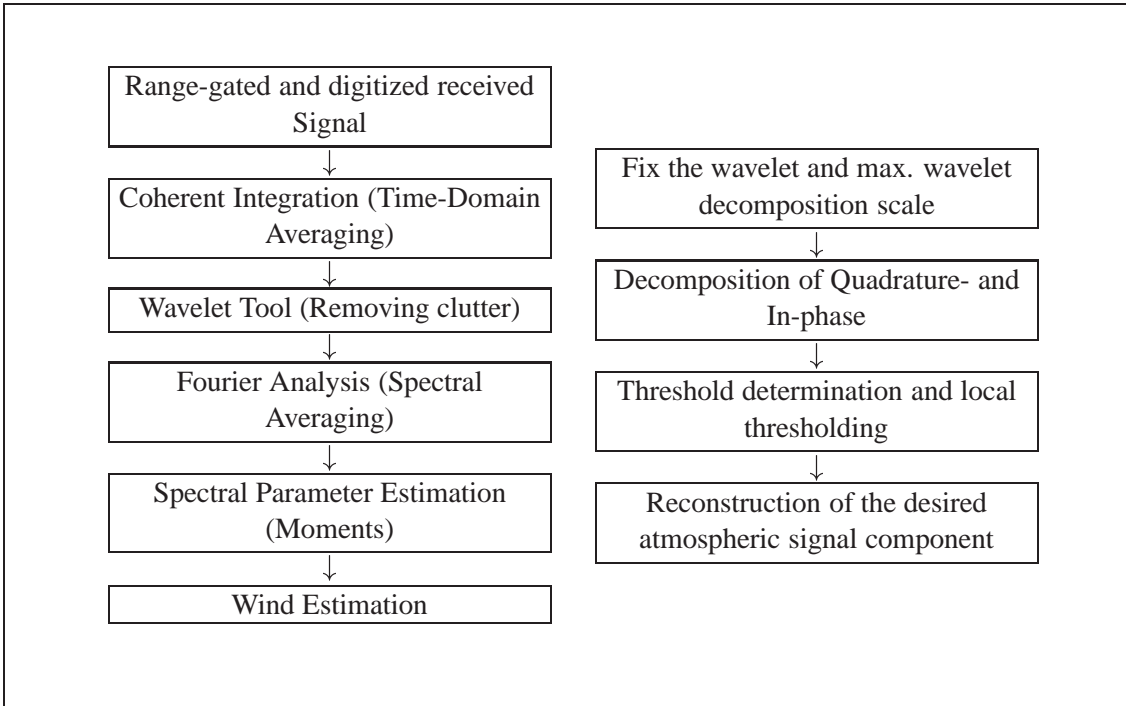


Figure 13: Left: The flow diagram extended by the wavelet tool. Right: The wavelet algorithm flow diagram.

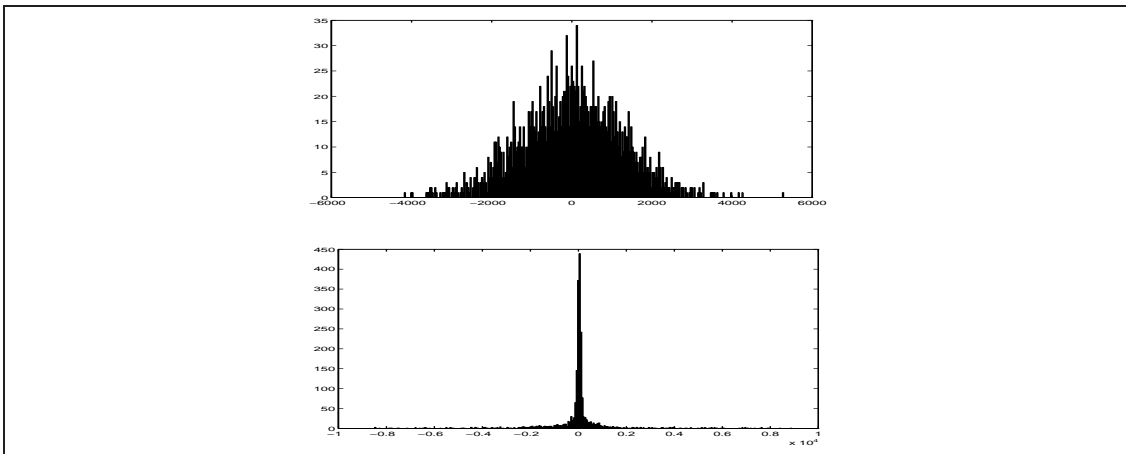


Figure 14: This Figure shows typical histograms of the wavelet coefficients (see text). The upper histogram represents an in-phase series without an airplane echo and the lower histogram represents an in-phase series with an airplane reflection.

clutter amplitude is much higher than the Doppler frequency amplitude. Because the algorithm removes the ground clutter completely, the reconstructed signal consists only of the atmospheric part (and some noise). This demonstrates impressively the difference of the nonlinear wavelet

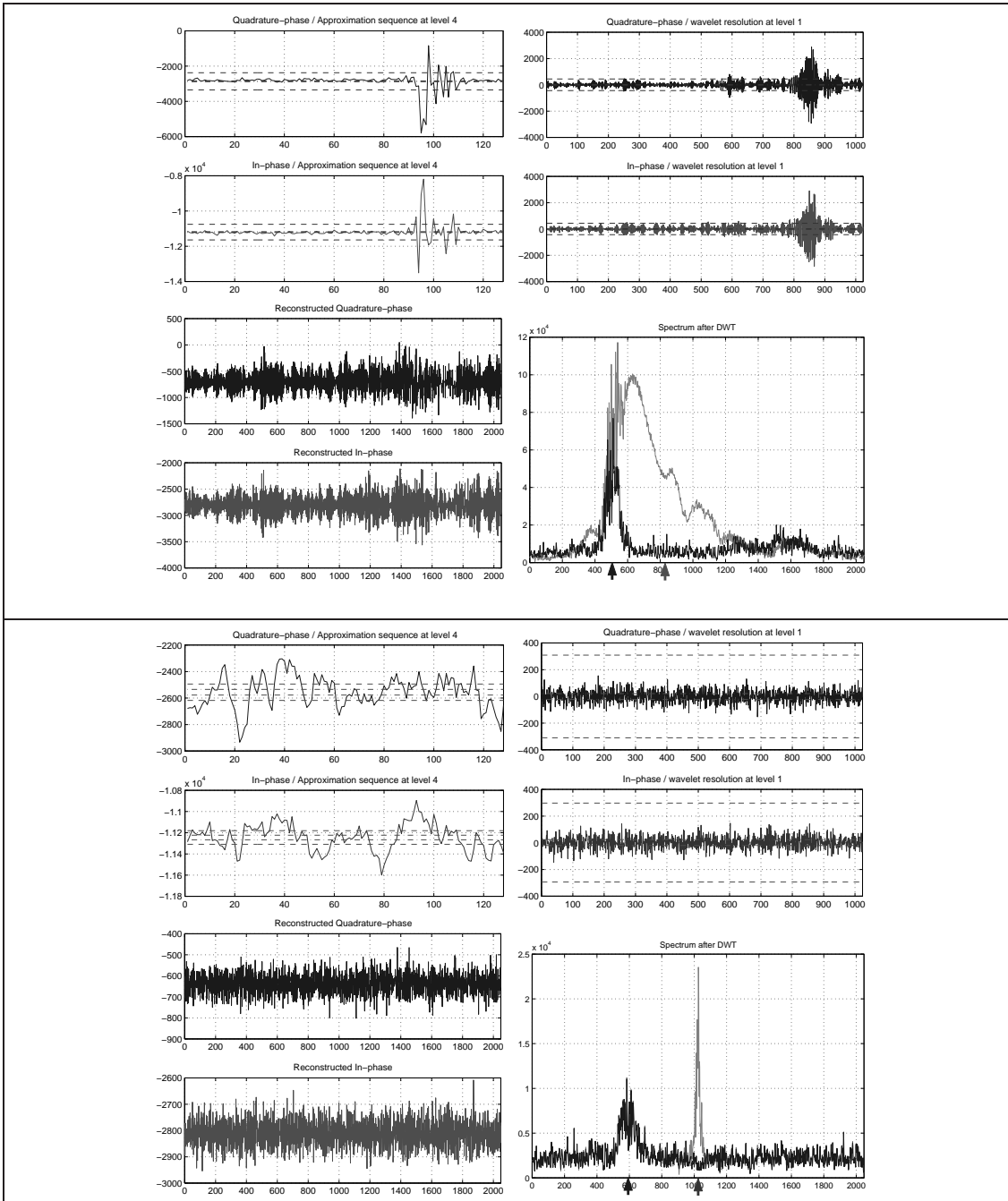


Figure 15: Decomposition ($\bar{\lambda}_k$ and $\bar{\gamma}_{1k}$), reconstruction and Fourier power spectrum of gate 17 (top) and gate 11 (below). The black curves in the power spectra representations display the decontaminated spectra. Clearly to recognize are the differences of moment estimations, see the computed first moment before (gray arrow) and after (black arrow) the filtering step.

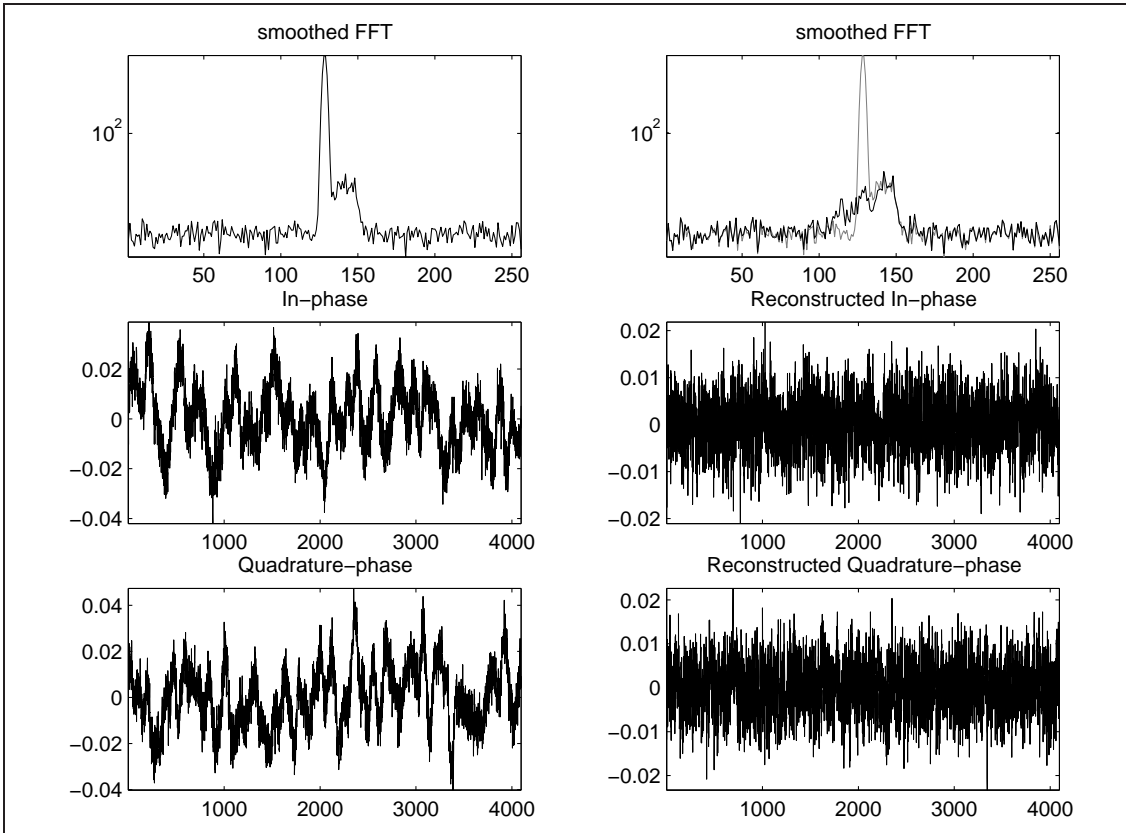


Figure 16: Top left: Simulated Fourier-power-spectrum with strong ground clutter influence and with an atmospheric signal overlapping the ground clutter peak. Lower left: I/Q time series derived from the simulated Fourier-power-spectrum using the [56] method. Lower right: I/Q time series after applying the nonlinear wavelet filter. Top right: Resulting Fourier-power-spectrum based on the reconstructed (filtered) signal.

filtering method compared to Fourier methods and digital filtering: The spectra of clutter and atmospheric signal can overlap as much as they want, nonetheless we can still separate the two components. The different amplitude of both signals allows the discrimination by thresholding.

For intermittent clutter, one of the distinct advantages of wavelet based techniques is certainly the ability to describe a transient signal with only a few wavelet coefficients. This is caused by the finite support of the wavelet basis. It is the localizing properties of wavelets, that makes the wavelet transform especially suited for filtering of transient signals.

To expose how the routine is acting on measured RWP time series we go back to the presented ‘real life’ problem (example Figure 11). We use this example to demonstrate the robustness of the method. The problem was that the signal at gate 17 was contaminated by intermittent clutter (aircraft echo) and the signal at gate 11 by persistent ground clutter. Using standard signal processing, the spectra were significantly biased and thus the moment estimation and finally the wind vector

reconstruction. Figure 15 shows exemplarily how wavelet thresholding was realized in decomposition sequences $\bar{\lambda}_k$ and $\bar{\gamma}_{1k}$ of gate 11 and 17. The dotted lines correspond to the thresholds. It can be observed that in both cases the clutter components have been removed completely.

References

- [1] R.A. Adams, *Sobolev Spaces*, Academic Press, New York, 1975.
- [2] J.-C. Boisse, V. Klaus and J.-P. Aubagnac, A wavelet transform technique for removing airplane echos from ST radar signals, *J. Atmos. Oceanic Technol.* **(16)** (1999), 334–346.
- [3] B. Borden, Mathematical problems in radar inverse scattering, *Inverse Problems* **18(1)** (2002), R1-R28.
- [4] D. Burgess and P.S. Ray, Principles of radar, in: *Mesoscale Meteorology and Forecasting*, AMS (1986), 85–117.
- [5] D.A. Carter, K.S. Gage, W.L. Ecklund, W.M. Angevine, P.E. Johnston, A.C. Riddle, J. Wilson and C.R Williams, Developments in UHF lower tropospheric wind profiling at NOAA's Aeronomy Laboratory, *Radio Science* **30(4)** (1995), 977–1001.
- [6] C.K. Chui, *An Introduction to Wavelets*, Academic Press, Boston, (1992).
- [7] A. Cohen and I. Daubechies, Non-separable bidimensional wavelet bases, *Rev. Mat. Iberoamericana* **9** (1993), 51–137.
- [8] A. Cohen, I. Daubechies and J. Feauveau, Biorthogonal bases of compactly supported wavelets, *Comm. Pure Appl. Math.* **45** (1992), 485–560.
- [9] C.E. Cook and M. Bernfeld, *Radar Signals*, Academic Press, New York, republished by Artech House, Norwood, MA, 1993 (1967).
- [10] S. Dahlke, P. Maass and G. Teschke, Reconstruction of wideband reflectivity densities by wavelet transforms, to appear in: *Adv. Comput. Math.*
- [11] S. Dahlke, P. Maass and G. Teschke, Reconstruction of reflectivity densities II: The narrow-band approach, submitted.
- [12] S. Dahlke and P. Maass, The affine uncertainty principle in one and two dimensions, *Comp. Math. Appl.* **(30)** (1995), 293–305.
- [13] I. Daubechies, Orthonormal bases of compactly supported wavelets, *Comm. Pure Appl. Math.* **41** (1987), 909–996.
- [14] I. Daubechies, *Ten Lectures on Wavelets*, CBMS–NSF Regional Conference Series in Applied Math. **61**, SIAM, Philadelphia, (1992).
- [15] R. DeVore, Nonlinear approximation, *Acta Numerica* **7** (1998), 51–150.

- [16] R.J. Duffin and A.C. Schaefer, A class of nonharmonic Fourier series, *Trans. Amer. Math. Soc.* **72** (1952), 341–366.
- [17] R.J. Doviak and D.S. Zrnić, *Doppler radar and weather observation*, Academic Press (1993).
- [18] D.L. Donoho, I.M. Johnstone, G. Kerkyacharian and D. Picard, Density estimation by wavelet thresholding, Technical Report, Dept. of Statistics, Stanford University (1993).
- [19] D.L. Donoho and I.M. Johnstone, Minimax estimation via wavelet shrinkage, Technical Report No. 402, Department of Statistics, Stanford University (1992).
- [20] E. Feig and C.A. Micchelli, L^2 synthesis by generalized ambiguity functions, in: *Multivariate Approximation IV*, C.K. Chui, W. Schempp and K. Zeller (Eds.), ISNM 90, Birkhäuser, Basel, (1989), 143–156.
- [21] K.S. Gage, C.R. Williams, W.L. Ecklund and P.E. Johnston, Use of two profilers during MC-TEX for unambiguous identification of Bragg scattering and Rayleigh scattering, *J. Atmos. Sci.* **56** (1999), 3679–3691.
- [22] E.E. Gossard and R.G. Strauch, *Radar Observations of Clear Air and Clouds*, Elsevier (1983).
- [23] E.E. Gossard, A fresh look at the radar reflectivity of clouds, *Radio Sci.* **14(6)** (1979), 1089–1097.
- [24] A. Grossmann, J. Morlet and T. Paul, Transforms associated to square integrable group representations, I. General results, *J. Math. Phys.* **26** (1985), 2473–2479.
- [25] C.F. Heil and D.F. Walnut, Continuous and discrete wavelet transforms, *SIAM Reviews* **31(4)** (1989), 626–666.
- [26] P.H. Hildebrand and R.S. Sekhon, Objective determination of the noise level in Doppler spectra, *J. Appl. Meteor.* **13(10)** (1974), 808–811.
- [27] W. Härdle and G. Kerkyacharian and D. Picard and A. Tsybakov, *Wavelets, Approximation, and Statistical Applications*, Springer, New York, (1998).
- [28] R.Q. Jia and C.A. Micchelli, Using the refinement equations for the construction of pre-wavelets II: Powers of two. In: *Curves and Surfaces*, P.J. Laurent, A. LeMéhauté and L.L. Schumaker (Eds.), Academic Press, New York, (1991), 209–246.
- [29] J.-P. Kahane and P.-G. Lemarié-Rieusset, *Fourier Series and Wavelets*, Gordon and Breach Science Publishers, Luxembourg, (1995).
- [30] G. Kaiser, *A Friendly Guide to Wavelets*, Birkhäuser, Boston, Basel, Berlin, (1994).
- [31] R.J. Keeler and R.E. Passarelli, Signal processing for atmospheric radars, in: *Radar in Meteorology*, American Meteorological Society, Boston, (1990), 199–229.
- [32] V. Lehman and G. Teschke, Wavelet based methods for improved wind profiler signal processing, *Annales Geophysicae* **19** (2001), 825–836.

- [33] A.K. Louis, P. Maass and A. Rieder, *Wavelets. Theory and Applications*, John Wiley, Chichester (1997).
- [34] R.N. McDonough and A.D. Whalen. *Detection of Signals in Noise*, Academic Press, second edition, (1995).
- [35] S. Mallat, Multiresolution approximation and wavelet orthonormal bases of $L^2(\mathbf{R})$, *Trans. Amer. Math. Soc.* **315** (1989), 69–88.
- [36] P. Maass, Wideband approximation and wavelet transform, in: *Proceedings of the IMA* **39**, F.A. Grünbaum et al. (Eds.), Springer, (1990), 83–88.
- [37] P.T. May and R.G. Strauch, An examination of wind profiler signal processing algorithms, *J. Atmos. Oceanic Technol.* **6(8)** (1989), 731–735.
- [38] D.A. Merritt, A statistical averaging method for wind profiler doppler spectra, *Journal of Atmospheric and Oceanic Technology* **12(5)** (1995), 985–995.
- [39] Y. Meyer, *Wavelets and Operators*, Cambridge Studies in Advanced Mathematics, vol. **37**, Cambridge, (1992).
- [40] H. Naparst, Radar signal choice and processing for dense target environment, Ph.D. thesis, University of California, Berkeley, (1988).
- [41] H. Naparst, Dense target signal processing, *IEEE Trans. Information Theory* **37(2)** (1991), 317–327.
- [42] F.M. Ralph, P.J. Neiman, D.W. van de Kamp and D.C. Law, Using spectral moment data from NOAA’s 404-MHz radar wind profilers to observe precipitation, *Bull. Amer. Meteorol. Soc.* **76(10)** (1995), 1717–1739.
- [43] F.M. Ralph, P.L. Neiman and D. Ruffieux, , Precipitation identification from radar wind profiler spectral moment data: Vertical velocity histograms, velocity variance, and signal power - vertical velocity correlation, *J. Atmos. Oceanic Technol.* **13** (1996), 545–559.
- [44] L. Rebollo–Neira, A. Plastino, and J. Fernandez–Rubio, Reconstruction of the joint time–delay Doppler–scale reflectivity density in a wide–band regime. A frame theory based approach, *J. Math. Phys.* **41(8)** (2000), 5325–5341.
- [45] A.W. Rihaczek, *High Resolution Radar*, McGraw–Hill, New York, (1969).
- [46] J. Röttger and M.F. Larsen, UHF/VHF radar techniques for atmospheric Research and wind profiler applications, in: *Radar in Meteorology*, *American Meteorological Society*, Boston, (1990), 235–281.
- [47] R. v. Sachs and B. MacGibbon, Nonparametric curve estimation by wavelet thresholding with locally stationary errors, Technical Report, Dept. of Math, University of Kaiserslautern (1998).
- [48] D. Sirmans and B. Bumgarner, Numerical comparisons of five mean frequency estimators, *J. Appl. Meteor.* **14** (1975), 991–1003.

- [49] G. Teschke, Waveletkonstruktion über Unschärferelationen und Anwendungen in der Signalanalyse, Ph.D. Thesis, University of Bremen, (2001).
- [50] T. Tsuda, Data acquisition and processing, in: *Middle Atmosphere Program - Handbook for MAP* **30** (1989), 151–183.
- [51] C.H. Wilcox, The synthesis problem for radar ambiguity functions, Technical Summary Report 157, United States Army, University of Wisconsin, (1960).
- [52] P. Wojtaszczyk, *A Mathematical Introduction to Wavelets*, Cambridge University Press, Cambridge, (1997).
- [53] R.F. Woodman, Spectral moment estimation in MST radars, *Radio Sci.* **20** (1985), 1185–1195.
- [54] R.F. Woodman and A. Guillen, Radar observations of wind and turbulence in the stratosphere and mesosphere, *J. Atmos. Sci.* **31** (1974), 493–505.
- [55] P.M. Woodward, *Probability and Information Theory, with Applications to Radar*, Pergamon Press, London, (1953).
- [56] D.S. Zrnić, Simulation of weatherlike Doppler spectra and signals, *J. Appl. Meteor.* **14** (1975), 619–620.